Entrainment and Dynamics of Ocean-derived Impurities within Europa's Ice Shell

J. J. Buffo[1,2], B. E. Schmidt[1], C. Huber[3], and C. C. Walker[4]

[1]Georgia Institute of Technology [2]Dartmouth College [3]Brown University [4]Woods Hole Oceanographic Institution

Corresponding author: Jacob Buffo (jacob.j.buffo@dartmouth.edu)

Key Points:

- Planetary ices contain a chemical fingerprint inherited from the thermochemical properties and dynamics of the parent liquid reservoir
- Observable thermochemical heterogeneities in Europa's ice shell can be used to infer the geophysical evolution of the shell
- Constraining material entrainment and transport within planetary ices will aid in assessing the habitability of icy ocean worlds

Abstract

Compositional heterogeneities within Europa's ice shell likely impact the dynamics and habitability of the ice and subsurface ocean, but the total inventory and distribution of impurities within the shell is unknown. In sea ice on Earth, the thermochemical environment at the ice-ocean interface governs impurity entrainment into the ice. Here, we simulate Europa's ice-ocean interface and bound the impurity load (1.053-14.72 ppt bulk ice shell salinity) and bulk salinity profile of the ice shell. We derive constitutive equations that predict ice composition as a function of the ice shell thermal gradient and ocean composition. We show that evolving solidification rates of the ocean and hydrologic features within the shell produce compositional variations (ice bulk salinities of 5-50% of the ocean salinity) that can affect ice's material properties. As the shell thickens, less salt is entrained at the ice-ocean interface, which implies Europa's ice shell is compositionally homogeneous below ~ 1 km. Conversely, the solidification of water filled fractures or lenses introduces substantial compositional variations within the ice shell, creating mechanically and thermally susceptible regions that could drive geological feature formation and evolution. Our results suggest that ocean materials entrained within Europa's ice shell impact the formation of geologic terrain and could be resolved by future spacecraft observations.

Plain Language Summary

Europa, the second innermost moon of Jupiter, likely houses an interior ocean that could provide a habitat for life. This ocean resides beneath a ~10-30 km thick ice shell which could act as a barrier or conveyor for ocean-surface material transport that could render the ocean chemistry either hospitable or unfavorable for life. Additionally, material impurities in the ice shell will alter its physical properties and thus affect the global dynamics of the moon's icy exterior. That said, few of the interior properties of the ice shell or ocean have been directly measured. On Earth, the composition of ocean-derived ice is governed by the chemistry of the parent liquid and the rate at which it forms. Here we extend models of sea ice to accommodate the Europa ice-ocean environment and produce physically realistic predictions of Europa's ice shell composition and the evolution of water bodies (fractures and lenses) within the shell. Our results show that the thermal gradient of the ice and the liquid composition affect the formation and evolution of geologic features in ways that will likely be detectable by future spacecraft (e.g. by ice penetrating radar measurements made by Europa Clipper).

1. Introduction

Europa's ocean was the first detected beyond Earth [*Khurana et al.*, 1998; *Kivelson et al.*, 2000]. Studies [*Cassen et al.*, 1979; *Pappalardo et al.*, 1999; *Ross and Schubert*, 1987; *Squyres et al.*, 1983] indicate that Europa's internal structure hosts a thick global ocean bounded by a silicate mantle below and a water ice shell above. These findings have fueled interest in the moon's interior dynamics, which may facilitate environments suitable for life (e.g. [*Board and Council*, 2012b; *Chyba and Phillips*, 2001; *Des Marais et al.*, 2008; *Reynolds et al.*, 1983; *Russell et al.*, 2017]). Europa's ice shell plays a crucial role in the moon's dynamics and evolution, as both a barrier and conveyer between the ocean and surface. Because most of the data available for Europa is derived from remote sensing techniques, the ice shell is a primary medium through which the properties of the ocean and interior can be understood, as the ice expresses how the body has evolved through its geology and composition. However, at present many of the ice shell's properties are not well constrained, including ice thickness, ice chemistry, and the distribution of shallow water [*Billings and Kattenhorn*, 2005; *Schmidt et al.*, 2011; *Walker and Schmidt*, 2015; *Zolotov and Shock*, 2001].

Constraining characteristics of the Europan environment, locating potentially habitable niches, understanding the transport processes supporting them, and investigating their connectivity are planned objectives of the Europa Clipper mission [*Phillips and Pappalardo*, 2014]. As such, quantifying the physical, thermal, chemical, and mechanical properties of the ice shell is imperative to understanding Europa's geophysical and material transport processes that control its habitability.

Heterogeneities in the ice shell have been linked to a number of proposed dynamic processes: solid state convection in the lower ice shell [*Han and Showman*, 2005; *Howell and Pappalardo*, 2018; *McKinnon*, 1999], subduction or subsumption of surface material [*Johnson et al.*, 2017b; *Kattenhorn*, 2018; *Kattenhorn and Prockter*, 2014], eutectic melting that may lead to the formation of chaos and lenticulae [*Manga and Michaut*, 2017; *Michaut and Manga*, 2014; *Schmidt et al.*, 2011], formation and sustenance of water bodies within the shell [*Kargel et al.*, 2000; *Zolotov and Kargel*, 2009]. Yet the process by and rate at which impurities are entrained within the ice remain poorly constrained, and while current models implement a range of potential impurity loads to test model sensitivity to variations in ice composition [*Han and Showman*, 2005; *Johnson et al.*, 2017a; *Pappalardo and Barr*, 2004] they do not predict ice composition directly. Furthermore, observations reveal that young, active terrain is richer in non-ice material than the average ice [*McCord et al.*, 2002] (Supplementary Figure S1), suggesting recent interaction with subsurface water reservoirs enriched with salts [*Manga and Michaut*, 2017; *Michaut and Manga*, 2014; *Schmidt et al.*, 2011], the effusion of ocean materials through fractures [*Fagents*, 2003], or melt through of a thin ice shell [*Greenberg et al.*, 1999].

When ice forms in an aqueous environment, it preserves a thermochemical record of the water from which it formed [*Feltham et al.*, 2006; *Gross et al.*, 1977; *Hunke et al.*, 2011; *Turner and Hunke*, 2015; *Untersteiner*, 1968]. For Europa, the ice shell grew from the freezing of, and is thus a window into, the ocean. With a geologically young surface ($<10^8$ yr [*Carr et al.*, 1998]) suggesting active ice shell overturn, dynamic regions of Europa's surface (e.g. bands and chaos) may harbor 'fossil ocean material' entrained in the ice shell as recently as 1Mya [*Howell and Pappalardo*, 2018]. This could provide an accessible sample of the contemporary ocean, as it is highly likely that Europa's ice, much like sea ice and marine ice on Earth, contains pockets and channels filled with brine, salts, gasses, and other impurities derived from the dynamics of freezing at the ice-ocean interface [*Eicken*, 2003; *Pappalardo and Barr*, 2004; *Zolotov and Kargel*, 2009; *Zotikov et al.*, 1980] (See Figure 1). On Earth, sea ice captures such a record of the thermochemical processes in the upper ocean during its formation. As the ocean solidifies, dissolved solutes are rejected as crystalline ice forms and a porous water-ice matrix filled with hypersaline interstitial fluid is produced [*Buffo et al.*, 2018; *Feltham et al.*, 2006; *Hunke et al.*, 2011; *Turner and Hunke*, 2015; *Untersteiner*, 1968; *Weeks and Lofgren*, 1967]. This process produces a compositionally-driven gravitational instability in the newly formed porous ice layer that results in buoyancy-driven convection of the denser pore fluid into the underlying liquid reservoir. Referred to as gravity drainage, this process has been observed to be the primary method of desalination during sea ice formation and has been successfully incorporated into a number of numerical models [*Buffo et al.*, 2018; *Griewank and Notz*, 2013; *Huppert and Worster*, 1985; *Turner and Hunke*, 2015; *Wells et al.*, 2011; *Worster*, 1991].

Quantifying the relationship between Europa's ice composition and interfacial thermochemistry at the time of formation would provide a technique for linking observed ice properties to characteristics of its origin liquid water reservoir (a 'frozen fingerprint' of the source water) and forecasting the properties of ice produced under diverse thermal and chemical

conditions – informing the synthesis of future mission data and geodynamic models. Impurities and structural heterogeneities within ice alter its thermal, physicochemical, and dielectric properties [*Feltham et al.*, 2006; *Hunke et al.*, 2011; *Weeks and Ackley*, 1986]. Thus, beyond the ice shell's chemistry, the dynamics of impurity entrainment will affect the potentially appreciable, and ongoing, hydrological activity within Europa's ice shell in the form of perched water lenses, fractures, dikes, and sills [*Manga and Michaut*, 2017; *Michaut and Manga*, 2014; *Schmidt et al.*, 2011; *Walker and Schmidt*, 2015]. Moreover, interpretation of measurements taken by Europa Clipper's ice penetrating radar, REASON, depend critically on ice composition and dielectric properties [*Blankenship et al.*, 2009; *Kalousová et al.*, 2017; *Weeks and Ackley*, 1986]. If the ice shell is impurity rich it has the potential to reflect and attenuate radar signals, which can be used to investigate the ice shell's interior structure but may also prevent observation of the ice-ocean interface [*Kalousová et al.*, 2017].

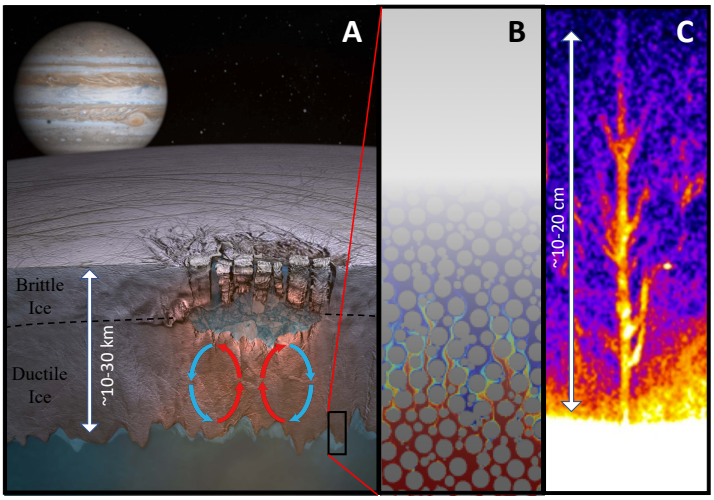

Figure 1 – The Europa ice-ocean system. A) A brittle ice lithosphere overlies a ductile ice mantle (dashed line) in contact with a subsurface ocean. A diapir generated perched water lens is an example of a putative hydrological feature within the ice shell that may facilitate the surface expression of recently entrained ocean material. **B)** Akin to terrestrial environments, the ice-ocean interface of Europa will likely be characterized by a two-phase ice-brine system, allowing solutes and other ocean material to be trapped within pore spaces. **C)** Brine channels in terrestrial sea ice. (Image Credit: A – Adapted from Britney Schmidt/Dead Pixel FX, UT Austin. B – Adapted from Joaquín Jiménez-Martínez http://petrelharp. github.io/asn_2016/asn-2016-talk.html C – Adapted from [*Worster and Rees Jones*, 2015])

To constrain the impurity load within Europa's ice shell and investigate the possible dynamics associated with the presence of salt in the ice shell, we constructed a one-dimensional reactive transport model adapted from the sea ice model of [*Buffo et al.*, 2018] for the Europa environment. We performed simulations of the formation and evolution of Europa's ice shell, validated against empirical observations of sea ice and marine ice growth rates and composition. The simulations include fluid and solute transport and the associated impurity entrainment that occurs at ice-ocean/brine interfaces. The model actively tracks the dynamic ice-ocean/brine interface as it propagates and catalogs the composition of the ice as it becomes impermeable and traps solutes within the ice. Since the ice composition derives from the initial ocean, we test an array of putative Europan ocean chemistries and thermal regimes and derive constitutive relationships between entrainment rates and the local thermal and chemical environment.

2. Methods

153 *2.1 Numerical Model*

154 The growth and evolution of the ice-ocean/brine interface is treated using an adapted
155 version of the one-dimensional, two-phase, reactive transport model of sea ice described by [*Buffo*
156 *et al.*, 2018]. Water/ice mass, energy, and salinity are conserved using a coupled set of equations
157 that combines mushy layer theory and the enthalpy method. The governing equations are:
158

159 $$\overline{\rho c}\frac{\partial T}{\partial t} = \left(\bar{k}\frac{\partial^2 T}{\partial z^2}\right) - \rho_{ice} L \frac{\partial \phi}{\partial t} \quad (1)$$

160

161 $$\phi\frac{\partial S_{br}}{\partial t} = \left(\bar{D}\frac{\partial^2 S_{br}}{\partial z^2}\right) - \frac{\rho_{ice}}{\rho_{br}} S_{br}\frac{\partial \phi}{\partial t} \quad (2)$$

162

163 $$H = c_{ice}T + L\phi \quad (3)$$

164

165 $$\phi = \begin{cases} 0 & H < H_s = c_{ice}T_m \\ (H - H_s)/L & -\ if\ - \quad H_s \le H \le H_s + L \\ 1 & H > H_s + L \end{cases} \quad (4)$$

166

167 where ρ is density, c is specific heat capacity, T is temperature, t is time, z is the vertical
168 coordinate, k is heat conductivity, L is the latent heat of fusion for the water to ice phase
169 transformation, ϕ is liquid fraction, S is salinity, D is salt diffusivity, H is enthalpy, H_s is the
170 enthalpy of a discretization cell consisting of only solid ice, and T_m is melting/freezing
171 temperature. Subscripts *ice* and *br* refer to characteristics of the ice and brine components of the
172 two-phase mixture, respectively, and variables carrying an over bar are volumetrically averaged
173 quantities (i.e. $\bar{y} = \phi y_{br} + (1 - \phi) y_{ice}$). Equations 1 and 2 ensure conservation of heat and mass,
174 respectively, and equations 3 and 4, combined, make up the enthalpy method. All variables and
175 values used throughout the text can be found in Table 1.

176 The desalination of forming ice is governed by brine expulsion and gravity drainage. Brine
177 expulsion refers to the phase change driven flux of hypersaline brine within the porous ice matrix
178 into the underlying liquid reservoir. As a volume containing both ice and brine components
179 continues to solidify, assuming incompressible flow, conservation of mass requires that brine must
180 be expelled from the volume. This is due to the density difference between ice and water. Given
181 the unidirectional solidification scenarios considered here, the brine will move downward into the
182 ambient ocean/brine. Gravity drainage refers to the buoyancy-driven convective overturn of brine
183 within the permeable multiphase layer. Both effects were considered by the model of Buffo et al.
184 (2018); however, in line with previous research [*Griewank and Notz*, 2013; *Wells et al.*, 2011],
185 gravity drainage was shown to be the primary mode of desalination. As such, with minimal loss
186 of accuracy, we forego simulating phase change driven Darcy flow (brine expulsion) in the porous
187 ice and opt to use the one-dimensional gravity drainage parameterization of [*Griewank and Notz*,
188 2013] to represent fluid transport. This parameterization represents the process of gravity drainage
189 through brine channels as a linear function of the local Rayleigh number, and is widely used for
190 solving multiphase melting/solidification problems [*Griewank and Notz*, 2013; *Turner and Hunke*,
191 2015; *Turner et al.*, 2013; *Wells et al.*, 2011]. Here, the mass of brine transported out of a
192 multiphase layer *j* is given as:

$$br_j^{\downarrow} = \alpha\left(Ra_j - Ra_c\right)dz^3dt = \alpha\left(\frac{g\rho_{sw}\beta\Delta S_j\widetilde{\Pi}h_j}{\kappa\mu} - Ra_c\right)dz^3dt \qquad (5)$$

where α is a constant of proportionality, Ra_j is the Rayleigh number of the *j*th layer, Ra_c is the critical Rayleigh number, *dz* and *dt* are the spatial and temporal discretization sizes, respectively, g is acceleration due to gravity, ρ_{sw} is the density of the ambient reservoir fluid (ocean/brine), β is a density coefficient describing the relationship between density and salinity, ΔS_j is the difference in salinity of the brine in the *j*th layer and the ambient ocean, h_j is the height of the *j*th layer above the basal surface of the ice, κ is the thermal diffusivity of seawater, μ is the kinematic viscosity of seawater, and $\widetilde{\Pi}_j$ is the minimum permeability of any layer between the *j*th layer and the basal ice surface. The permeability function given by Griewank and Notz (2013) is utilized, and a critical porosity cutoff is implemented to prevent drainage from layers containing low liquid fractions (here $\phi < 0.05$ [*Golden et al.*, 2007] results in a layer's fluid transport being shut off). Heat and salt are transported out of the model domain by this convective process and the equations of mushy layer theory (Eq. 1 & 2) are modified accordingly (See [*Buffo et al.*, 2018] for details). Equations 1-4 are solved using an implicit finite difference method and a standard second order spatial discretization for the diffusion terms to produce spatiotemporal profiles of temperature, salinity, and porosity at the ice-ocean interface.

For this work, we update the model of *Buffo et al.* [2018] to include active interface tracking. Modeling the entire ice shell thickness and lifespan at the resolution needed to capture the reactive transport dynamics occurring near the ice-ocean/brine interface is computationally intractable. To overcome these difficulties, we modified our model [*Buffo et al.*, 2018] such that it actively tracks only the permeable or 'active' region of the ice shell, determined by the critical porosity where fluid flow ceases (e.g. [*Golden et al.*, 1998; *Golden et al.*, 2007]). In the top-down solidification scenarios modeled, when the fluid fraction of a discretized layer drops below the critical porosity it is removed from the active domain and its properties are cataloged, along with all the cells above it, and an equal number of replacement layers are added to the bottom of the domain with ambient ocean/brine characteristics ($T_{oc}, S_{oc}, \rho_{sw}$). This enables the efficient simulation of much thicker regions of ice growth (10s-100s of meters vs. 10s-100s of centimeters) over much longer times (10s-1000s of years vs. 10s-100s days) by removing 'dead' cells which are no longer interacting with the underlying ocean. This is a novel addition to existing reactive transport models of ocean-derived ices (e.g. [*Cox and Weeks*, 1988; *Griewank and Notz*, 2013; *Turner et al.*, 2013]) and specifically resolves the difficulty of accurately simulating the physicochemical evolution of thick planetary ices.

Symbol	Definition	Value	Units
$\boldsymbol{\alpha}$	1D Advection Coefficient	1.56 x 10^{-1}	kg m^{-3} s^{-1}
$\boldsymbol{\beta}$	Density (Salinity) Coefficient	5.836 x 10^{-4}	kg ppt^{-1}
$\boldsymbol{br^{\uparrow,\downarrow}}$	Vertical Brine Transport	Calculated	kg
$\boldsymbol{c_{br}}$	Brine Heat Capacity	3985	J kg^{-1} K^{-1}
$\boldsymbol{c_{ice}}$	Ice Heat Capacity	2000	J kg^{-1} K^{-1}
$\boldsymbol{D}$	Salt Diffusivity	Calculated	m^2 s^{-1}
$\boldsymbol{g}$	Acceleration Due to Gravity	1.32/9.8	m s^{-2}
$\boldsymbol{h}$	Distance to Interface	Calculated	m
$\boldsymbol{H_{shell}}$	Ice Shell Thickness	Varies	m
$\boldsymbol{H}$	Enthalpy	Calculated	J kg^{-1}

$\boldsymbol{H_S}$	Enthalpy of Solid Cell	Calculated	J kg $^{-1}$
$\boldsymbol{k_{br}}$	Brine Heat Conductivity	0.6	W m $^{-1}$ K $^{-1}$
$\boldsymbol{k_{ice}}$	Ice Heat Conductivity	2	W m $^{-1}$ K $^{-1}$
$\boldsymbol{\kappa}$	Thermal Diffusivity	Varies	m ^{2} s $^{-1}$
$\boldsymbol{L, L_f}$	Latent Heat of Fusion	334,774	J kg $^{-1}$
$\boldsymbol{\lambda}$	Coefficient Dependent on $\boldsymbol{St}$	Calculated	-
$\boldsymbol{\mu}$	Kinematic Viscosity	1.88 x 10 $^{-3}$	m ^{2} s $^{-1}$
$\boldsymbol{\phi}$	Liquid Fraction	Calculated	-
$\boldsymbol{\phi_c}$	Critical Porosity	0.05	-
$\boldsymbol{\Pi}$	Permeability	Calculated	m ^{2}
$\boldsymbol{Ra}$	Rayleigh Number	Calculated	-
$\boldsymbol{Ra_c}$	Critical Rayleigh Number	1.01 x 10 $^{-2}$	-
$\boldsymbol{\rho_{br}}$	Brine Density	Varies	kg m $^{-3}$
$\boldsymbol{\rho_{ice}}$	Ice Density	917	kg m $^{-3}$
$\boldsymbol{\rho_{sw}}$	Ocean/Reservoir Density	Varies	kg m $^{-3}$
$\boldsymbol{S}$	Salinity	Calculated	ppt
$\boldsymbol{S_{lim}}$	Minimum Salinity	Varies	ppt
$\boldsymbol{S_{oc}}$	Ocean/Reservoir Salinity	Varies	ppt
$\boldsymbol{S_{tot}}$	Bulk Salinity/Total Salt	Calculated	ppt
$\boldsymbol{St}$	Stefan Number	Calculated	-
$\boldsymbol{t}$	Time	-	s
$\boldsymbol{T}$	Temperature	Calculated	K
$\boldsymbol{T_0}$	Supercooled Temperature	Varies	K
$\boldsymbol{T_1}$	Liquid Temperature	Varies	K
$\boldsymbol{T_m}$	Melting/Freezing Temperature	Varies	K
$\boldsymbol{T_{oc}}$	Ocean Temperature	Varies	K
$\boldsymbol{T_s}$	Surface Temperature	100	K
$\boldsymbol{v_m}$	Freezing Front Velocity	Calculated	m s $^{-1}$
$\boldsymbol{x_m}$	Freezing Front Position	Calculated	m
$\boldsymbol{z}$	Vertical Coordinate	-	m

Table 1 – Variables. All variables used in the text, along with their definition, values, and units.

2.2 The Stefan Problem: Deriving the Constitutive Equations

The interpolation of results used to derive the constitutive relationships between ice characteristics and the thermochemical environment hinges on the ability to fit the simulated data to a predefined function. The form of this function should be representative of the physical processes occurring within the simulation. As the equations governing the multiphase reactive transport model do not lend themselves to an analytical solution, it is logical to seek a simplified system that does. To investigate the evolution of dissolved salt in an ice-ocean environment we make a number of simplifying assumptions and solve Equation 2 analytically.

The classic Stefan problem describes the dynamics and evolution of pure substance melting/solidification and is well documented in the literature [*Huber et al.*, 2008; *Michaut and Manga*, 2014; *Rubinšteĭn*, 2000]. The basic geometry of the problem can be seen in Supplementary Figure S2. The analytical solution of the thermal profile in the solid and the time dependent solidification front is [*Huber et al.*, 2008]:

$$T(x,t) = T_0 - (T_0 - T_1)\frac{\mathrm{erf}\left(\frac{x}{2\sqrt{\kappa t}}\right)}{\mathrm{erf}(\lambda)} \qquad (6)$$

$$x_m(t) = 2\lambda\sqrt{\kappa t} \tag{7}$$

$$\lambda \exp(\lambda^2)\,\mathrm{erf}(\lambda) = \frac{St}{\sqrt{\pi}} = \frac{c(T_0 - T_1)}{L_f\sqrt{\pi}} \tag{8}$$

where $T(x,t)$ is the temperature within the solid at position x and time t, T_0 is the temperature at the undercooled surface and is lower than the melting temperature of the solid, T_1 is the temperature of the liquid, κ is the thermal diffusivity of the solid, x_m is the position of the solidification front, λ is a coefficient depending on St, erf is the error function, St is the Stefan number defined as $St = c(T_0 - T_1)/L_f$, c is the specific heat of the solid, and L_f is the latent heat of fusion for the water-ice phase transition.

While the Stefan problem represents a simpler system than that of our reactive transport model, the underlying physics governing solidification are the same and similar behavior is to be expected. It has been suggested that the amount of impurities entrained in forming ice is related to the rate at which the ice forms [*Nakawo and Sinha*, 1984; *Weeks and Ackley*, 1986; *Zolotov and Kargel*, 2009]. Equations 6-8 can be utilized to investigate the relationships between the rate of ice formation and both the freezing front position and local thermal gradient. First, differentiating Equation 7 with respect to time gives:

$$v_m(t) = \dot{x}_m(t) = \frac{\lambda\kappa}{\sqrt{\kappa t}} = \frac{2\lambda^2\kappa}{x_m(t)} \tag{9}$$

$$\Rightarrow \quad v_m(t) \propto \frac{1}{x_m(t)} \tag{10}$$

where $v_m(t)$ is the solidification front velocity, which is equivalent to the rate of ice formation. This suggests that the rate of ice formation is inversely proportional to the position of the solidification front. Second, differentiating Equation 6 with respect to position gives:

$$\frac{\partial T(x,t)}{\partial x} = -\frac{(T_0 - T_1)}{\mathrm{erf}(\lambda)}\frac{1}{\sqrt{\pi\kappa t}}\exp\left(-x^2/4\kappa t\right) \tag{11}$$

At the position of the solidification front, $x_m(t) = 2\lambda\sqrt{\kappa t}$, Equation 11 becomes:

$$\frac{\partial T(x_m,t)}{\partial x} = -\frac{(T_0 - T_1)}{\mathrm{erf}(\lambda)}\frac{1}{\sqrt{\pi\kappa t}}\exp\left(-\lambda^2\right) \tag{12}$$

From Equation 9 we see that $\sqrt{\kappa t} = \lambda\kappa/v_m(t)$. Substituting this result into Equation 12 gives:

$$\frac{\partial T(x_m,t)}{\partial x} = -\frac{(T_0 - T_1)}{\mathrm{erf}(\lambda)}\frac{1}{\sqrt{\pi}\lambda\kappa}\exp\left(-\lambda^2\right)v_m(t) \tag{13}$$

$$\Rightarrow \quad \frac{\partial T(x_m, t)}{\partial x} \propto v_m(t) \tag{14}$$

Suggesting that the rate of ice formation is directly proportional to the local thermal gradient at the solidification front. The relationships derived in Equations 10 & 14 provide insight into the spatiotemporal evolution of the Stefan problem and its dependence on the local thermal environment. These results will be utilized below, where a modified Stefan problem (inclusion of a solute and fluid dynamics) is described and an analytical solution is derived. This solution describes the spatial and temporal distribution of the solute and provides the functional form of the constitutive equations used throughout the text.

To investigate the evolution of dissolved salt in an ice-ocean environment we make a number of simplifying assumptions and solve Equation 2 analytically. Assuming top-down unidirectional solidification of a salty ocean (e.g. sea ice, Europan ocean solidification) the evolution of salt in the system can be described by the equations of reactive transport (Equation 2 including the gravity drainage parameterization, with *br* subscripts dropped from *S* terms for simplicity):

$$\phi \frac{\partial S}{\partial t} = \left(\overline{D} \frac{\partial^2 S}{\partial z^2} \right) - \frac{\rho_{ice}}{\rho_{br}} S \frac{\partial \phi}{\partial t} + br_j^{\downarrow} \frac{\partial S}{\partial z} \tag{15}$$

where $br_j^{\downarrow}$ is the brine velocity in the *j*th layer described by the one-dimensional gravity drainage parameterization. Introducing a new coordinate, ξ, such that $\xi = z - z_m(t)$, places the origin at the ice-ocean interface and constitutes a moving coordinate system. In this new coordinate system Equation 15 can be written as:

$$\phi \frac{\partial S}{\partial \xi}\frac{\partial \xi}{\partial t} = \overline{D} \left[\frac{\partial^2 S}{\partial \xi^2} \left(\frac{\partial \xi}{\partial z} \right)^2 + \frac{\partial S}{\partial \xi}\frac{\partial^2 \xi}{\partial z^2} \right] - \frac{\rho_{ice}}{\rho_{br}} S \frac{\partial \phi}{\partial \xi}\frac{\partial \xi}{\partial t} + br_j^{\downarrow} \frac{\partial S}{\partial \xi}\frac{\partial \xi}{\partial z} \tag{16}$$

Rearranging Equation 16:

$$-\overline{D} \left[\frac{\partial^2 S}{\partial \xi^2} \left(\frac{\partial \xi}{\partial z} \right)^2 + \frac{\partial S}{\partial \xi}\frac{\partial^2 \xi}{\partial z^2} \right] - br_j^{\downarrow} \frac{\partial S}{\partial \xi}\frac{\partial \xi}{\partial z} + \phi \frac{\partial S}{\partial \xi}\frac{\partial \xi}{\partial t} = -\frac{\rho_{ice}}{\rho_{br}} S \frac{\partial \phi}{\partial \xi}\frac{\partial \xi}{\partial t} \tag{17}$$

Taking the appropriate spatial and temporal derivatives of ξ and substituting their values into Equation 17 gives:

$$-\overline{D} \frac{\partial^2 S}{\partial \xi^2} - \left(br_j^{\downarrow} + \phi v_m(t) \right) \frac{\partial S}{\partial \xi} = v_m(t) \frac{\rho_{ice}}{\rho_{br}} S \frac{\partial \phi}{\partial \xi} \tag{18}$$

For simplicity, we assume that $\phi(\xi) = \mathcal{H}(\xi)$, where $\mathcal{H}(\xi)$ is the Heaviside step function. While this is indeed a simplification, as it represents the mushy layer as an infinitesimally thin regime, the general liquid fraction profile of evolving sea ice demonstrates similar structure (See Figures 5-7 of Buffo et al., 2018). Substituting $\phi(\xi) = \mathcal{H}(\xi)$ into Equation 18 results in a simplified conservation of mass equation in the moving coordinate system:

$$-\overline{D}\frac{\partial^2 S}{\partial \xi^2} - \left(br_j^{\downarrow} + \phi v_m(t)\right)\frac{\partial S}{\partial \xi} = v_m(t)\frac{\rho_{ice}}{\rho_{br}} S\delta(\xi) \tag{19}$$

where $\delta(\xi)$ is the delta function. Equation 19 can be solved using Fourier transforms. Let the transform variable be χ, such that:

$$S(\chi) = \mathcal{FT}[S(\xi)] = \int_{-\infty}^{\infty} S(\xi)\exp(-i2\pi\chi\xi)\, d\xi \tag{20}$$

$$S(\xi) = \mathcal{FT}^{-1}[S(\chi)] = \int_{-\infty}^{\infty} S(\chi)\exp(i2\pi\chi\xi)\, d\chi \tag{21}$$

Applying the Fourier transform to Equation 19 gives:

$$4\pi^2\chi^2\overline{D}\, S(\chi) - i2\pi\chi\left(br_j^{\downarrow} + \phi v_m(t)\right)S(\chi) = v_m(t)\frac{\rho_{ice}}{\rho_{br}} S(\xi = 0, t) \tag{22}$$

Equation 22 has the solution:

$$S(\chi) = S(\chi, t) = \frac{v_m(t)\frac{\rho_{ice}}{\rho_{br}} S(\xi = 0, t)}{4\pi^2\chi^2\overline{D} - i2\pi\chi\left(br_j^{\downarrow} + \phi v_m(t)\right)} \tag{23}$$

Taking the inverse Fourier transform of Equation 23 gives:

$$S(\xi, t) = \int_{-\infty}^{\infty}\left[\frac{v_m(t)\frac{\rho_{ice}}{\rho_{br}} S(\xi = 0, t)}{4\pi^2\chi^2\overline{D} - i2\pi\chi\left(br_j^{\downarrow} + \phi v_m(t)\right)}\right]\exp(i2\,\pi\chi\xi)\, d\chi \tag{24}$$

$$= \frac{v_m(t)\frac{\rho_{ice}}{\rho_{br}} S(\xi = 0, t)}{\left(br_j^{\downarrow} + \phi v_m(t)\right)}\left[\pm 1 \mp \exp\left(\frac{-\pi\xi\left(br_j^{\downarrow} + \phi v_m(t)\right)}{\overline{D}}\right)\right] \tag{25}$$

Throughout this work we seek constitutive equations that relate the amount of salt entrained in forming ice to depth and local thermal gradient. Using the relationships of Equations 10 & 14, the definition of $\xi = z - z_m(t)$, and assuming in the active mushy layer near the ice-ocean interface, where reactive transport is possible, $z \sim z_m(t)$, we can rewrite Equation 25 in two forms:

$$S_{tot}(z_m) \propto \frac{1}{z_m}[1 - \exp(-z_m)] \tag{26}$$

$$S_{tot}\left(\frac{\partial T}{\partial z}\right) \propto \frac{\frac{\partial T}{\partial z}}{1 + \frac{\partial T}{\partial z}}\left[1 - \exp\left(-1/\frac{\partial T}{\partial z}\right)\right] \tag{27}$$

where the first term on the right-hand side of each equation is a diffusion term which dominates at later times (deeper depths, lower thermal gradients) and the second term is an advection-reaction term which dominates at early times (shallower depths, larger thermal gradients). Together, Equations 26 & 27 provide the functional forms for the constitutive equations produced throughout the remainder of the text.

3. Results

3.1 Salt Entrainment on Earth

Two types of ice present on Earth provide the best end-member analogs for Europa's ice shell: sea ice and marine ice. Here, sea ice refers to frozen seawater at the ocean's surface, while marine ice is seawater-derived ice which has accreted onto the basal surface of meteoric ice shelves (e.g. [*Zotikov et al.*, 1980]). While both ices form via the directional solidification of seawater, and thus undergo the same dynamics during their formation, they form under different thermal regimes, resulting in unique compositional and physical structure. Sea ice provides the upper limit of impurity entrainment and an ideal analog for ice formed along steep thermal gradients near Europa's surface, as its formation is driven by rapid heat loss to the cold polar atmosphere. Fortunately, there exists nigh on a century's worth of observations and quantitative measurements regarding vertical heterogeneities in the thermal, chemical, and microstructural properties of sea ice [*Malmgren and Institutt*, 1927]. With the proximity of the 100 K surface, if the Europan ice shell is ever tens to hundreds of meters thick, or if any shallow liquid water bodies are emplaced at such depths within the ice shell, these regions will experience similarly high thermal gradients, suggesting high impurity uptake exceeding even that of sea ice. We have previously modeled the annual growth of sea ice to study its thermochemical evolution and ability to record variations in ocean characteristics through the reproduction of ice core properties [*Buffo et al.*, 2018]. This model was adapted to actively track the advancing ice-ocean interface and accommodate potentially diverse ocean chemistries. In Figure 2, we re-validate our approach by comparing sea ice simulations to empirical measurements of depth dependent sea ice bulk salinity [*Nakawo and Sinha*, 1981; *Notz and Worster*, 2009]. We show that actively tracking the evolution of the ice-ocean interface and simulating small-scale solute transport within the porous ice produces bulk salinity profiles that agree well with observations. We achieve salinity profiles that exhibit the characteristic 'c-shape' typical of first-year sea ice, represented by the 'MARCH' profile of Figure 2b [*Malmgren and Institutt*, 1927], and reproduce the bulk salinity values observed in the field. Based on the constitutive relationship between depth and bulk salinity (Eq. 10), we use an inverse fit to the simulated values to extend the profile to the upper portion of the ice where extreme temperature gradients affect numerical stability when using a Neumann boundary condition. Thus, our model captures the physical processes that occur during ice formation in high thermal gradient environments, which will govern the formation of ice near Europa's surface.

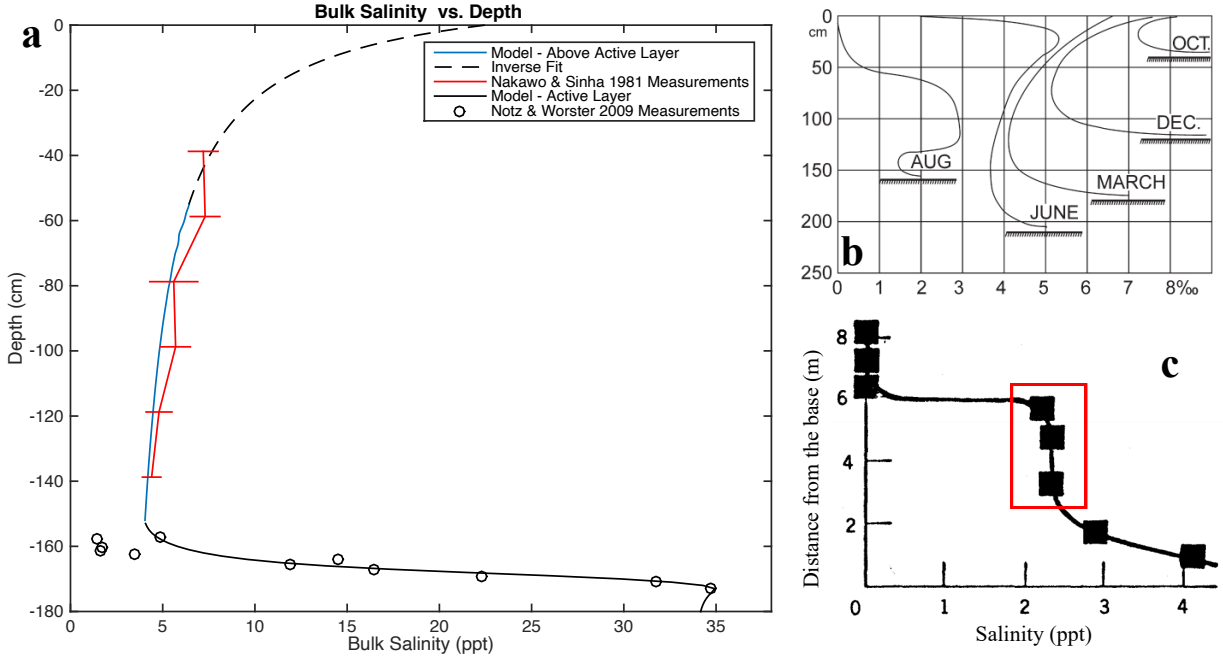

Figure 2: Salinity profiles within observed and modeled marine and sea ice. a) Modeled (blue and black solid lines), empirical (red line [*Nakawo and Sinha*, 1981] and black circles [*Notz and Worster*, 2009]), and interpolated (black dashed line) bulk salinity profiles of sea ice. The numerical model assumes a preexisting 50 cm thick layer of sea ice in conductive equilibrium (linear temperature profile) with an atmospheric temperature of 250K and an ocean temperature of 271.5K. A conductive heat flux is maintained throughout the simulation at the upper boundary. The model was run for 1.5×10^7 sec (~174 days, a typical sea ice annual cycle) with a time step of 100 sec. The dashed line is the product of a Levenberg-Marquardt algorithm fit to the function $S(z)=a+b/(c-z)$, where S is bulk salinity, z is depth, and a, b, and c are constants, applied to the modeled bulk salinities above the active layer (blue solid line). While all of the bulk salinity values (blue and black solid lines) are a byproduct of the same model simulation, values in the active layer (black solid line) are excluded from the Levenberg-Marquardt fit (black dashed line) as the constitutive equations (Table 3) are derived assuming an infinitesimally thin mushy layer. **b)** Typical first-year sea ice salinity profiles have a characteristic 'c' shape where the bulk salinity evolves over the season due to material transport and ice growth (from [*Malmgren and Institutt*, 1927]). **c)** Bulk salinity measurements from the bottom 8 m of an ice core extracted from the Ross Ice Shelf by [*Zotikov et al.*, 1980]. The bottom 6 m is accreted marine ice, with the 'asymptotic region' outlined in red approaching diffusive equilibrium during ice formation (image modified from [*Zotikov et al.*, 1980]).

Most of Europa's ice shell (below about 1 km), however, will have formed and evolved under low thermal gradient conditions. As thermal gradients decrease, ice composition approaches an asymptotic lower limit governed by the critical porosity of the active layer when it is in diffusive equilibrium with the underlying ocean. Here, critical porosity is analogous to a percolation threshold, where regions with porosities below this limit are no longer hydraulically connected to the surrounding pore network and any remaining salt is trapped in discrete brine pockets. A similar environment to the bulk of Europa's ice shell exists at the base of deep ice on Earth where marine ice is formed (e.g. [*Zotikov et al.*, 1980]). This unique, and less studied, variety of ocean-derived ice forms on the basal surface of terrestrial ice shelves due to much lower thermal gradients than typical open ocean sea ice (e.g. ~10 K/m for surficial sea ice; ~0.08 K/m for marine ice [*Zotikov et al.*, 1980]) leading to greatly reduced growth rates of ~2 cm/yr [*Zotikov et al.*, 1980]. While the thermal gradients present in the marine ice system (~0.08 K/m) exceed the upper estimates for a thin (5-10 km) Europan ice shell (~0.02 K/m) [*McKinnon*, 1999; *Mitri and Showman*, 2005], even

at this higher thermal gradient impurity entrainment has already approached its lower limit – characterized by asymptotic bulk salinity profiles, shown in Figure 2c. This makes marine ice the best terrestrial analog of Europan ice formed in the low thermal gradient regime. Adopting a critical porosity of $\phi_c = 0.05$, based on observations of sea ice permeability [*Golden et al.*, 1998; *Golden et al.*, 2007], and assuming an ocean salinity, $S_{oc} = 34\ ppt$, the theoretical lower limit for salt entrainment into terrestrial ice (diffusive equilibrium when impermeability is reached) is given by $S_{lim} = \phi_c S_{oc} = 1.70\ ppt$. The average bulk salinity of the 'asymptotic region' seen in Figure 2c is 2.32 ppt. Utilizing the constitutive equation for bulk salinity versus thermal gradient derived in the next section for terrestrial seawater in the diffusive regime (dT/dz = 0.08 K/m), a bulk salinity of 1.95 ppt is predicted. The difference of 0.37 ppt between the observed and predicted bulk salinity values translates to a 16% error, attributed to small variations in unconstrained parameters, such as critical porosity and permeability-porosity relationships (both of which can appreciably affect impurity entrainment rates [*Buffo et al.*, 2018]). The efficiency of brine migration through the porous ice lattice and the threshold at which percolation is possible are poorly constrained [*Golden et al.*, 1998; *Golden et al.*, 2007; *Wells et al.*, 2011] but govern the dynamics of multiphase flow, brine retention in the ice, and ultimately ice composition. At the ice-ocean/brine interface, reduced permeability or a larger critical porosity would lead to more salt being entrained in the ice. Alternately, enhanced permeability, a smaller critical porosity, or the dearth of a percolation threshold (e.g. due to melt transport along ice grain boundaries [*McCarthy et al.*, 2013; *McCarthy et al.*, 2019]) would result in less salt entrainment. Nevertheless, our model closely reproduces observations of sea ice, and the same multiphase reactive transport physics applied in low-thermal gradient conditions match observations of marine ice composition, which capture broadly the two thermochemical regimes that ice on Europa is expected to occupy.

3.2 The Effects of Thermal Gradient and Ocean Chemistry on Ice Composition

Aside from the different surface temperature (<110 K vs ~250 K), gravity (1.32 vs 9.81 m/s^2) and potential compositional characteristics between Europa and Earth, one of the largest differences is sheer scale of the ice. While the majority of sea ice exhibits a maximum thickness of <10 m [*Kurtz and Markus*, 2012; *Laxon et al.*, 2013] (ice drafts have been known to exceed 25 m and reach up to 47 m beneath pressure ridges [*Davis and Wadhams*, 1995; *Lyon*, 1961]) and marine ice accretion occurs at depths <1.5 km [*Craven et al.*, 2009; *Galton‐Fenzi et al.*, 2012; *Zotikov et al.*, 1980], Europa's ice shell is likely 10-30 km thick [*Billings and Kattenhorn*, 2005; *Nimmo et al.*, 2003; *Tobie et al.*, 2003]. It is important to note, however, that despite differences in ice thickness, all ice-ocean interfaces will remain at or near their pressure melting points, which for a 1.5 km thick terrestrial ice shelf is comparable to an ~11.1 km thick Europan ice shell.

Model runs are initiated with the domain completely filled by one of the ocean chemistries investigated at a temperature just above its freezing point (Supplementary Section S1). The top boundary is governed by a Neumann boundary condition with a no-flux condition set for salt and it is assumed that the overlying ice is in conductive thermal equilibrium [*McKinnon*, 1999] (i.e. $dT/dz = (T_{oc} - T_S)/H_{shell}$). The bottom boundary is governed by a Dirichlet boundary condition and is simulated as being in contact with an infinite ambient ocean/brine reservoir ($T_{oc}, S_{oc}, \rho_{sw}$) (for additional information on code functionality see [*Buffo et al.*, 2018]).

To construct the full ice shell from discrete model runs, several simulations at various depths (solidification front locations) run in parallel, and the results are combined to produce the constitutive relationships that relate ice composition to its thermochemical environment at the time of formation. It is important to note that the top-down unidirectional solidification of Europa's ice

shell from a quiescent ocean is likely a simplification as the aqueous differentiation of its juvenile planetesimal was likely a tumultuous and complex process [*Kargel et al.*, 2000]. However, this formation scenario was selected as it mirrors the formation of sea and marine ice, the only benchmarks available for the formation of ocean-derived ices and provides the simplest case which enables the derivation of the upper limit of salt possible in Europa's ice shell. Moreover, the functional forms of the constitutive equations are derived under such conditions, requiring simulations of this type to derive the bulk salinity-thermal gradient relationships paramount to the remainder of the manuscript (e.g. basal fracture and perched lens solidification).

Composition of the ocean is critical to ice formation because of the relationship between the salinity of water and its freezing point. The conductive nature of Europa's ocean [*Khurana et al.*, 1998; *Kivelson et al.*, 2000], as well as spectral measurements [*McCord et al.*, 1999], suggests the presence of dissolved salts, but nearly all of its intrinsic properties (thickness, composition, structure) remain poorly constrained. Potential Europan ocean chemistries have been explored in a number of studies [*Marion et al.*, 2005; *McKinnon and Zolensky*, 2003; *Vance et al.*, 2019; *Zolotov and Kargel*, 2009; *Zolotov and Shock*, 2001]. Here we implement the chemistry proposed by [*Zolotov and Shock*, 2001], who assumed that Europa's ocean formed during its differentiation via partial aqueous extraction from bulk rock with the composition of CV carbonaceous chondrites (Table 2). Alternate formation materials (e.g. CI chondrites [*Zolotov and Kargel*, 2009]) will alter the predicted ionic composition of the ocean, and variable molecular diffusivities, atomic masses, and v'ant Hoff factors may affect impurity entrainment rates in associated ocean-derived ices. For comparison, we also considered an ocean composition identical to terrestrial seawater (Table 2). Well-known liquidus curves exist for terrestrial seawater [*Commission*, 2010]. However, the freezing behavior of potentially more exotic Europan ocean compositions is comparatively less well known, so we constructed a new software package, Liquidus 1.0, to derive quadratic liquidus curves for any chemistry supported by the equilibrium chemistry package FREZCHEM 6.2, which includes a wide range of material properties for the expected non-ice components of brines (Supplementary Section S1).

Species	Terrestrial Seawater (mol/kg)	Europan Ocean (mol/kg)
Na^+	4.69×10^{-1}	4.91×10^{-2}
K^+	1.02×10^{-2}	1.96×10^{-3}
Ca^{2+}	1.03×10^{-2}	9.64×10^{-3}
Mg^{2+}	5.28×10^{-2}	6.27×10^{-2}
Cl^-	5.46×10^{-1}	2.09×10^{-2}
SO_4^{2-}	2.82×10^{-2}	8.74×10^{-2}
Total Salt (ppt)	34	12.3

Table 2 – Ocean compositions. List of ion species and relative abundances for terrestrial seawater [*Dickson and Goyet*, 1994] and the proposed Europan ocean chemistry of [*Zolotov and Shock*, 2001].

We forego simulating the possible precipitation of hydrated salts (e.g. mirabilite ($Na_2SO_4 \cdot 10H_2O$) [*Butler et al.*, 2016], epsomite ($MgSO_4 \cdot 7H_2O$), meridianiite ($MgSO_4 \cdot 11H_2O$) [*McCarthy et al.*, 2011; *McCarthy et al.*, 2007]) for two reasons. First, implementing reactive transport modeling to simulate the evolution of ice-ocean worlds is a relatively novel approach, thus it is logical to begin with the simpler ice-brine binary system (as opposed to the ice-brine-hydrate ternary system), to both validate the approach and obtain a first order understanding of how salts are entrained in planetary ices. Second, the low thermal gradients experienced

throughout much of the shell will facilitate slow ice growth, allowing for the dissipation of salt from high salinity regions via both convection and diffusion, preventing saturation and precipitation. Future work investigating ternary systems could reveal additional bulk salinity profile structure in the shallow ice shell and other high thermal gradient environments brought about by the precipitation of such hydrated salts. We discuss the potential geophysical implications of salt hydrates in the context of intrusive hydrological features (basal fractures and perched water bodies) in Sections 3.3.2 and 3.3.3.

We simulated Europa's ice shell growth at eight discrete ice thicknesses (10 m, 50 m, 75 m, 100 m, 150 m, 200 m, 250 m, and 300 m), for four different hypothetical ocean compositions (Europan Ocean 12.3 ppt/100 ppt/282 ppt and Terrestrial Seawater 34 ppt). By the time the ice shell reaches 300 m in thickness the thermal gradient at the ice-ocean interface is shallow enough that the bulk salinity curve becomes asymptotic and variations in the salt entrainment rate will be minimal at all greater depths. This asymptotic lower limit is set by the ocean composition and critical porosity ($S_{lim} = \phi_c S_{oc}$). Simulations of larger ice thicknesses (>300 m) were therefore excluded, given the predicted ice composition below 300 m would vary by <1 ppt (see the first row of Table 3 and the following paragraph). Europan ocean concentrations were selected to bound the best estimates available from theory and observation: a rigorous estimate provided by theoretical calculations is 12.3 ppt [*Zolotov and Shock*, 2001], while the saturation point of the same fluid would reach an ocean salinity of 282 ppt, and the upper limit based on the Galileo magnetometer data is a salinity of 100 ppt [*Hand and Chyba*, 2007]. The results for all ocean compositions can be seen in Figure 3 and Supplementary Figure S4. The results are depth-dependent and thermal gradient-dependent bulk salinity profiles, which are then interpolated using a Levenberg-Marquardt algorithm fit to the constitutive equations, the explicit form of which, including the coefficients needed to accommodate stretches and translations, are shown in Table 3.

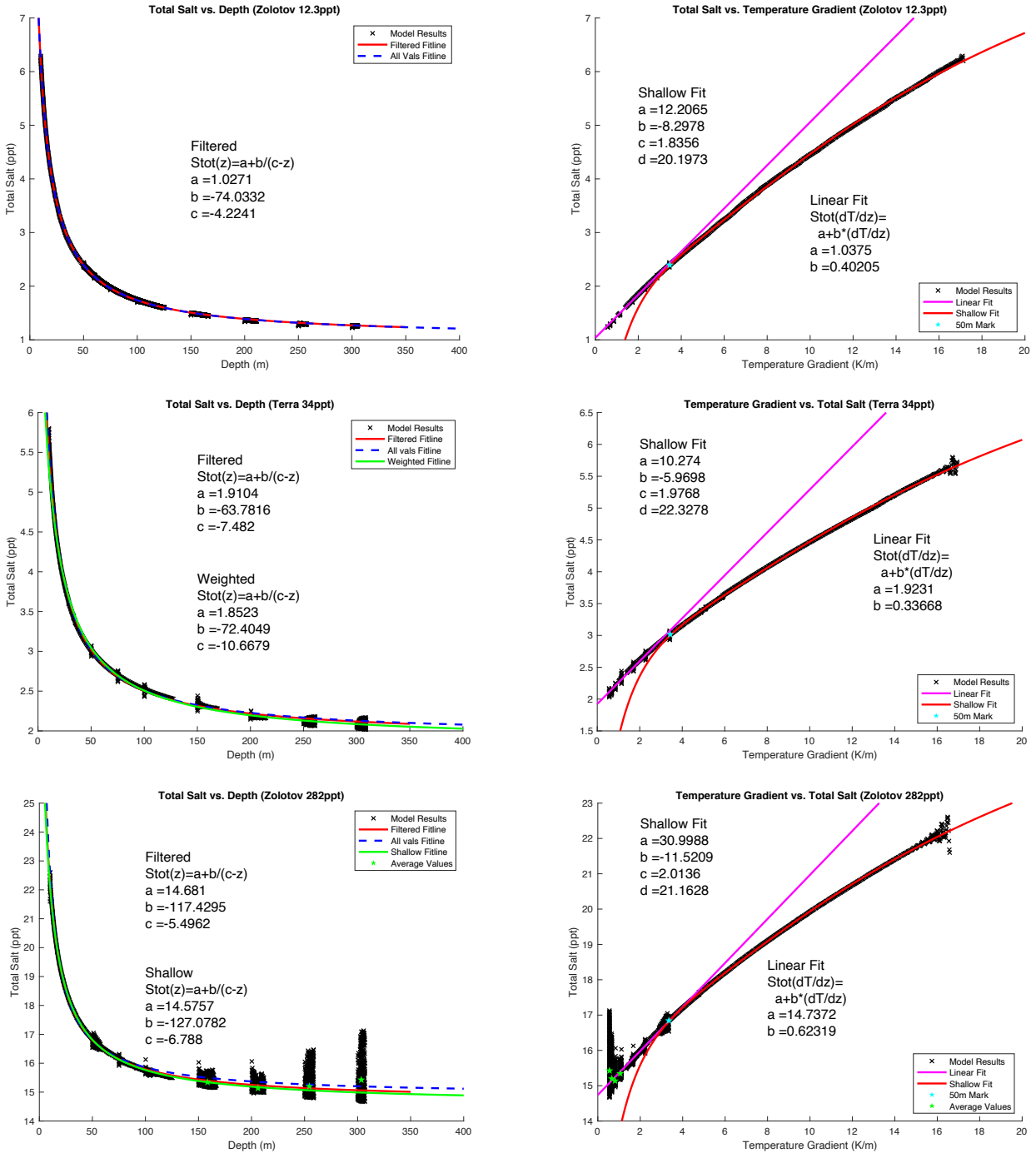

Figure 3: Simulations of depth dependent and thermal gradient dependent bulk salinity for three different ocean chemistries (100 ppt simulation is presented in Figure S4) Relationships are fit by the constitutive equations of Table 3. **Left Column,** Model results [black exes] (numerical dispersion at the onset of each run has been removed) and original (all values), filtered (numerical dispersion at run onset removed), weighted (where applicable – weighted by data density), and shallow (where applicable – fitting model results from 10-200 m runs) fit lines [blue dashed line, red line, and green lines, respectively]. **Right Column,** Simulated results [black exes] as well as linear and 'Shallow' (See Table 3) fit lines [pink and red lines, respectively]. Green stars represent average bulk salinity for an entire run at a given depth – highlighting that the majority of the simulated data lies near the fit lines, even when scatter is present. Blue stars identify the thermal gradient associated with a 50 m depth within an equilibrated conductive ice shell, which is the transition point between the diffusive and advective-reactive regimes.

Constitutive Equation	a	b	c	d
$S_{tot}(z) = a + \frac{b}{(c - z)}$	$a_{12.3}$=1.0271 a_{100}=5.38 a_{282}=14.681 a_{34}=1.8523	$b_{12.3}$=-74.0332 b_{100}=-135.096 b_{282}=-117.429 b_{34}=-72.4049	$c_{12.3}$=-4.2241 c_{100}=-8.2515 c_{282}=-5.4962 c_{34}=-10.6679	
$S_{tot}\left(\frac{\partial T}{\partial z}\right) = a + b\frac{\partial T}{\partial z}$	$a_{12.3}$=1.0375 a_{100}=5.4145 a_{282}=14.737 a_{34}=1.9231	$b_{12.3}$=0.40205 b_{100}=0.69992 b_{282}=0.62319 b_{34}=0.33668		
(Shallow Fit Line) $S_{tot}\left(\frac{\partial T}{\partial z}\right) = a + \frac{b\left(\frac{\partial T}{\partial z} + c\right)}{1 + \frac{\partial T}{\partial z}}\left[1 - exp\left(\frac{-d}{\partial T/\partial z}\right)\right]$	$a_{12.3}$=12.21 a_{100}=22.19 a_{282}=31.00 a_{34}=10.27	$b_{12.3}$=-8.30 b_{100}=-11.98 b_{282}=-11.52 b_{34}=-5.97	$c_{12.3}$=1.836 c_{100}=1.942 c_{282}=2.014 c_{34}=1.977	$d_{12.3}$=20.20 d_{100}=21.91 d_{282}=21.16 d_{34}=22.33

Table 3: Constitutive Equations. The reactive transport model results are fit by constitutive equations relating bulk salinity to shell depth and temperature gradient for each of the ocean compositions, column 1, and their associated coefficients, a-d. Subscripts 12.3, 100, 282, and 34 refer to Europan ocean compositions with concentrations of 12.3 ppt, 100 ppt, 282 ppt, and terrestrial seawater with a concentration of 34 ppt, respectively. These equations provide a parameterization of Europa's ice shell composition's dependence on the local thermal environment at the time of ice formation, which can be utilized to provide efficient first order estimates of the properties of ice formed in a variety of chemical and thermal environments without the need for explicit simulation.

The translation of the model from the Earth system to Europa hinges on the observation that as thermal gradients near the ice-ocean/brine interface decrease ice bulk salinity asymptotically approaches a lower limit governed by molecular diffusion in the pore fluid (Figure 2c). The result of this asymptotic behavior is twofold. First, the ice shell will experience ice-ocean interface thermal gradients below those found on Earth during much of its formation. This suggests a relatively homogeneous ice layer (formed in the asymptotic regime) underlying a thin (~1 km), compositionally distinct surficial layer (formed under steep thermal gradients). This stratification would produce variations in the thermochemical and mechanical properties of these layers, potentially introducing a boundary along which rheological transitions (e.g. brittle lid vs. ductile mantle) and transport regimes (conduction vs. convection) may be promoted. Second, the lower portion of the contemporary ice shell is believed to be ductile enough to undergo solid state convection [*Barr and McKinnon*, 2007; *Han and Showman*, 2005; *McKinnon*, 1999; *Tobie et al.*, 2003], providing a mechanism that would mix this region of the shell, homogenizing it chemically and flattening its thermal profile (consider the analogous geothermal profile). A convective thermal profile in this ductile region suggests an ice-ocean interface subject to very low thermal gradients [*Mitri and Showman*, 2005], implying that accreted ice salinities would be at or near their lower limit, irrespective of ice thickness. Thus, the ductile region of the contemporary ice shell should have a bulk composition at or near the lower limit set by the critical porosity. Such a compositional profile varies negligibly from those predicted by the unidirectional solidification scenarios we simulate here (below 1 km predicted salinities vary by <150 ppm from the theoretical lower limit). Any heterogeneities in impurity entrainment would require associated ice-ocean heat flux variations (e.g., ocean driven heating of the ice shell [*Soderlund et al.*, 2014], thermochemical diapirism [*Pappalardo and Barr*, 2004], spatiotemporal variations in basal heat flux due to downwelling cold ice and/or the evolution of tidal heating within the ice shell [*Tobie et al.*, 2003]) with amplitudes large enough to appreciably affect entrainment rate. Notably, this implies that for much of the ice shell it is not the thermal regime of the ice but rather its critical porosity and permeability which will determine ice composition.

In general, the bulk salinity profiles and their corresponding relationships to depth within the ice shell and local temperature gradients are well-represented by our derived constitutive equations, suggesting that their functional forms (Eq. 26 & 27) capture much of the reactive transport physics that govern how ice forms in the presence of dissolved materials, and the movement of this material via advection and diffusion while the ice is still permeable. The division of impurity entrainment rate into two distinct thermal regimes, diffusive (low) and advective-reactive (high), is well accommodated and justified by the terrestrial benchmarks above. While there exist uncertainties in the limit of extreme thermal gradients ($\gg 20\ K/m$) and large salinities (e.g. scatter observed for the 282 ppt ocean at low thermal gradients, a consequence of salinity's increased sensitivity to changes in porosity at high ocean concentrations [Supplementary Section S5]), the high thermal conductivity of ice relative to water quickly diffuses such thermal anomalies. In conductive thermal equilibrium, 9 m of ice separating a 100 K surface and 273 K ocean does not support thermal gradients in excess of 20 K/m. Thus, after a thin layer of ice (<10 m) has formed the ice-ocean interface is substantially insulated and the constitutive can be confidently applied. Moreover, the results demonstrate that, as expected, the bulk salinity in the ice approaches the diffusive equilibrium limit under low thermal gradients. Thus, as perhaps the first quantitative estimate of impurity content, the constitutive equations derived here allow us to investigate the properties and evolution of Europa's ice shell and hydrological features contained therein.

3.3 The Evolution of Europa's Ice Shell

3.3.1 Total Salt

The constitutive equations derived above can be used to estimate the total salt content of Europa's ice shell prior to the onset of solid-state convection, producing an upper limit on the total impurity load of the ice shell. For these calculations, we assume a 25 km thick ice shell with an inner radius of 1,535 km and an outer radius of 1,560 km. The total salt content for a given ocean composition can be calculated by integrating the constitutive equation over the volume of the ice shell given the coefficients in Table 3. For an ice shell with inner radius R_1 and outer radius R_2,:

$$Total\ Salt\ in\ Shell = \frac{\rho_{ice}}{1000}\int_V S_{tot}(z)dV \qquad (28)$$

where ρ_{ice} is the density of ice, V is the volume of the ice shell, and $S_{tot}(z)$ is the constitutive equation relating bulk salinity and depth (Table 3). Rewriting z in terms of the spherical coordinate r, gives:

$$Total\ Salt\ in\ Shell = \frac{\rho_{ice}}{1000}\int_{R_1}^{R_2}\int_0^{2\pi}\int_0^{\pi}\left[a + \frac{b}{(c-(R_2-r))}\right] r^2 \sin\varphi\, dr\, d\theta\, d\varphi \qquad (29)$$

where a, b, and c are coefficients from the ocean/brine specific constitutive equation and (r, θ, φ) represent a spherical coordinate system.

The total volume of the 25 km thick Europan ice shell is ~7.5235 x 10^{17} m^3, while the approximate collective volume of Earth's oceans is ~1.332 x 10^{18} m^3 [*Charette and Smith*, 2010]. For the Europan ocean composition (Table 2), with concentrations of 12.3 ppt, 100 ppt, and 282 ppt the total salt entrained in a 25 km shell is 7.2894 x 10^{17} kg, 3.6633 x 10^{18} kg, and 1.0189 x 10^{19}

kg, respectively. This corresponds to average ice shell salinities (total salt/ice shell mass) of 1.0565 ppt, 5.3099 ppt, and 14.769 ppt, respectively. For a terrestrial ocean composition with a concentration of 34 ppt the total salt entrained in a 25 km shell is 1.2978 x 10^{18} kg, corresponding to an average ice shell salinity of 1.8811 ppt. For comparison, Earth's oceans contain ~4.5288 x 10^{19} kg of salt.

Directly related to the composition and bulk salinity of the ice is its density. Crucial in driving any potential solid-state convection on Europa, compositional buoyancy may either help or hinder large scale, thermally driven convective overturn in the ice shell. Horizontal density gradients have also been proposed as a driver of putatively observed subduction/subsumption on Europa's surface [*Johnson et al.*, 2017b; *Kattenhorn*, 2018]. Mirroring the profiles of bulk salinity, there exists a rapid and asymptotic decrease in ice density with depth for all ocean chemistries (Supplementary Figure S5), and subsequently throughout much of the shell the density is nearly homogeneous (e.g. for a 100 ppt Europan ocean chemistry ρ_{500m}=922.54 kg/m^3 and ρ_{25km}=922.25 kg/m^3). Our results demonstrate that, apart from a geophysically thin surface layer, significant variations in density with depth are unlikely to form as the ice shell freezes out. The maximum salt content predicted in the near surface is ~36 ppt (or ~3.6%), calculated by extending the constitutive equation relating bulk salinity and shell depth for the 282 ppt ocean to the surface ($z = 0$). The same calculation for the 100 ppt, 34 ppt, and 12.3 ppt oceans results in near surface salt contents of ~22 ppt, ~9 ppt, and ~19 ppt (or ~2.2%, ~0.9%, and ~1.9%), respectively. A number of these values are greater than, or close to, the 2% salt content needed to drive the subduction of certain laterally compositionally heterogeneous slabs calculated by [*Johnson et al.*, 2017a]. However, the physical, thermal, and chemical characteristics of the ice shell likely act in concert to control Europa's dynamics, as the material properties of ice are structurally, thermally, and chemically dependent (Supplementary Section S2). The expected salinity profile, along with the total impurity load, provides context on the nature of liquid and solid phases within the ice shell. Combined with thermal variations due to convection, tidal heating, or heat transfer from the ocean [*Howell and Pappalardo*, 2018; *Mitri and Showman*, 2005] and variations in physical properties such as porosity and viscosity [*Barr and McKinnon*, 2007; *Johnson et al.*, 2017a], more explicit constraints on the thermophysical formation of many of Europa's surface features are thus possible.

3.3.2 Basal Fractures

The fundamental processes that occur during the freezing of ice are not only applicable to the ocean, but to any water within the ice shell. We adapted our approach to accommodate the geometry of simple basal fractures (Supplementary Section S3), to investigate the composition of fractures upon re-freezing. Akin to the basal fractures of terrestrial ice shelves, fractures at the ice-ocean or other ice-liquid interface of Europa could either locally stabilize or destabilize the ice shell; they have the potential to suture the shell back together with newly frozen oceanic material [*Khazendar et al.*, 2009], or to propagate further, potentially penetrating to the surface [*Bassis and Walker*, 2011]. Such fractures appear within Europa's chaos terrain [*Collins and Nimmo*, 2009; *Walker and Schmidt*, 2015], a potential indicator of near-surface water reservoirs [*Schmidt et al.*, 2011] and a potential pathway for shallow water to make it to the surface in the form of plumes [*Sparks et al.*, 2017] (See Figure 1a).

We modeled basal fractures at both Europa's ice-ocean interface and a hypothetical ice-lens interface (Figure 4). The fractures are filled with fluid from the underlying reservoir (ocean or lens) and the fluid is assumed to remain well mixed during the simulations since the advective

timescale for rejected brine with a density 1 kg m^{-3} greater than the ambient fluid through a 25 km fracture is <1 day (equating gravitational and viscous drag forces for a parcel of brine near the crack tip of width $\mathcal{O}(1)$, $v \sim \Delta\rho g/\eta$). Due to the high aspect ratio of the basal fractures (penetration depth/basal width) we modeled them as solidifying horizontally inward, akin to how terrestrial magmatic dikes form, forced by the conductive profile of the ice shell into which the fracture is emplaced. The injection of water into the ice shell produces regions of very high thermal gradients between the relatively warmer water and cold ice. As a result, fractures refreeze to form ice wedges with chemically gradated composition, due to the amplified solidification rates at the fracture's edges and tip. Bulk salinity estimates of the most rapidly formed ice, near the walls of the fractures, have been excluded from Figure 4 (e.g. the dark blue layer seen in panel 4d). Thermal gradients in this region are > 20 K/m and exceed the range under which the constitutive equations were derived. Furthermore, under rapid solidification there is the potential for salt hydrates to precipitate and be trapped within the ice [*McCord et al.*, 2002; *Thomas et al.*, 2017], further altering its bulk salinity, thermophysical and mechanical properties. Due to the complex and metastable evolution of hydrate precipitation [*Chu et al.*, 2016; *Toner et al.*, 2014] we forego its simulation during the current investigation, but note that the bulk salinity of the most distal ice is expected to approach that of the fluid filling the basal fracture (i.e. increased salt retention upon flash freezing).

While these simulations do not completely capture all of the inherently two-dimensional structure and ternary phase evolution of the fracture (especially near the crack tip) these results currently provide the most realistic evaluation of basal fracture physicochemical evolution. The results suggest that basal fractures are geologically short-lived, at least in the upper shell, due to their high aspect ratios and rapid heat loss to the surrounding ice. At depth their lifetime may be extended by deformation processes brought about by tidal forces [*Nimmo and Gaidos*, 2002] or the presence of a warmer ductile ice layer [*Barr and McKinnon*, 2007; *Tobie et al.*, 2003]. While it is unlikely that fractures in the shallow shell contain liquid water for long, we show that the rapid injection and refreezing of saline fluid within a colder ice shell produces local chemical heterogeneities along the fracture walls that could preserve the fracture. Two important implications arise: the high salinity regions along the fracture walls produce a gradient in mechanical properties, potentially weakening the center of the fracture or concentrating stress here, while at the same time these regions could be more easily melted during reactivation of the fracture even in the absence of water from the ocean. Both of these provide mechanisms by which features can remain active even once they refreeze.

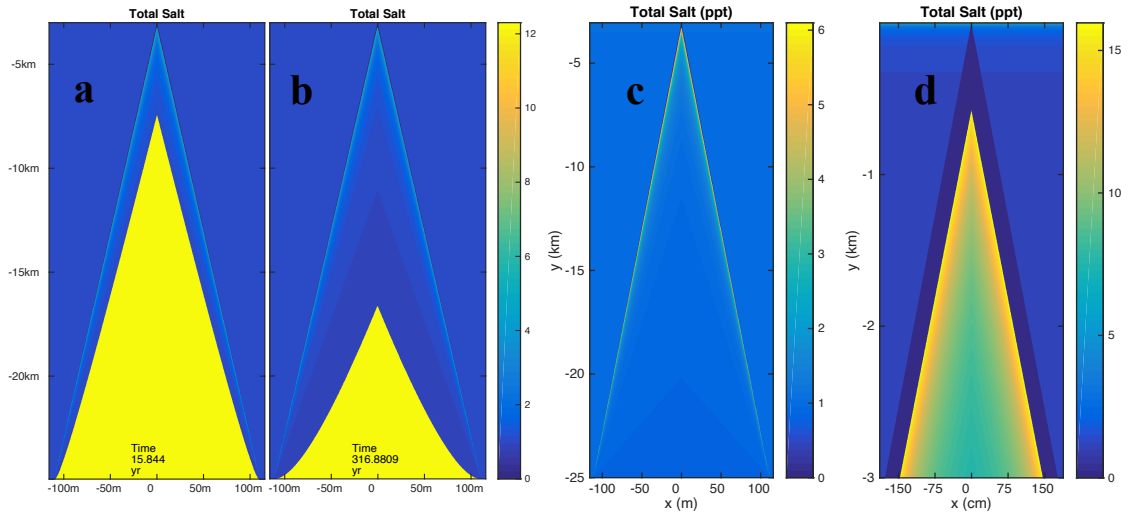

Figure 4: **Basal ice fractures refreeze to produce a gradient in salinity.** Temporal evolution of a hypothetical basal fracture, **a-b** (Supplementary Figures S7-8 and Sections S3-4), shows that rapid refreezing occurs, down to 5km within 15 years if the fracture can be held open over this timeframe. Profiles for deep fractures from the ice-ocean interface, **c** (due to 2 MPa stress in a 25 km shell; Depth – 21.925 km, Width – 220.9 m), and fractures from shallow lens interfaces, **d** (due to 2 MPa stress in a 3 km lid, Depth – 2.922 km, Width – 3.53 m), show similar patterns of high salt content along the fracture wall and toward the tip, and lower salinity toward the interior and base. These results show that gradients in mechanical properties are likely toward the surface where tidally modulated activity is more likely. For fractures from the ocean, the majority of the ice formed in the interior of the fracture, however, will have a salinity that is nearly indistinguishable from the bulk Europa ice. This suggests that fractures are likely to be regions of local discontinuities in ice shell properties, and potentially regions of weakness within the ice shell created by interfaces between salt and ice grains.

3.3.3 Brines within the Ice

Knowing the composition of the ice provides the chance to evaluate the formation, evolution, and longevity of water or brine systems within Europa's ice shell. For example, shallow lenses of liquid water are suggested to form *in situ* via melting of the ice shell [*Schmidt et al.*, 2011] (Figure 1a) or by injection through diking processes [*Manga and Michaut*, 2017; *Michaut and Manga*, 2014]. For such a lens, assuming the ice shell derived from a 34 ppt terrestrial ocean chemistry, letting the diffusive limit govern ice bulk salinity as shown above ($S_{lim} = \phi_c S_{oc}$) and tracking the evolving lens salinity, upon top down refreeze a 2 km thick lens located 1 km beneath a 100 K surface will produce ice compositions ranging from 0.0946 to 14.10 ppt. Additionally, upon complete refreeze, impurity rejection leads to the precipitation of an approximately 2.23 m layer of salt (likely in the form of a salt hydrate), assuming a saturation limit of 282 ppt (Figure 5). This 'salting out' process during the freezing of eutectic brines has been observed in terrestrial systems (e.g. British Columbia's hypersaline lakes [*Renaut and Long*, 1989]), and provides an efficient segregation mechanism that results in relatively pure ice overlying saturated brine in which basal salt hydrate layers precipitate [*Brown et al.*, 2020; *Buffo*, 2019].

Thus, impurity entrainment and rejection during freezing produce compositional heterogeneities within the ice shell and introduce a concentration process capable of producing salt/salt hydrate layers within the shell that have highly distinct mechanical, thermal, and dielectric properties. The ability to predict compositional variations around putative hydrological features in

731 Europa's shell will both constrain how these features form and inform spacecraft observations
732 [*Blankenship et al.*, 2009; *Kalousová et al.*, 2017].

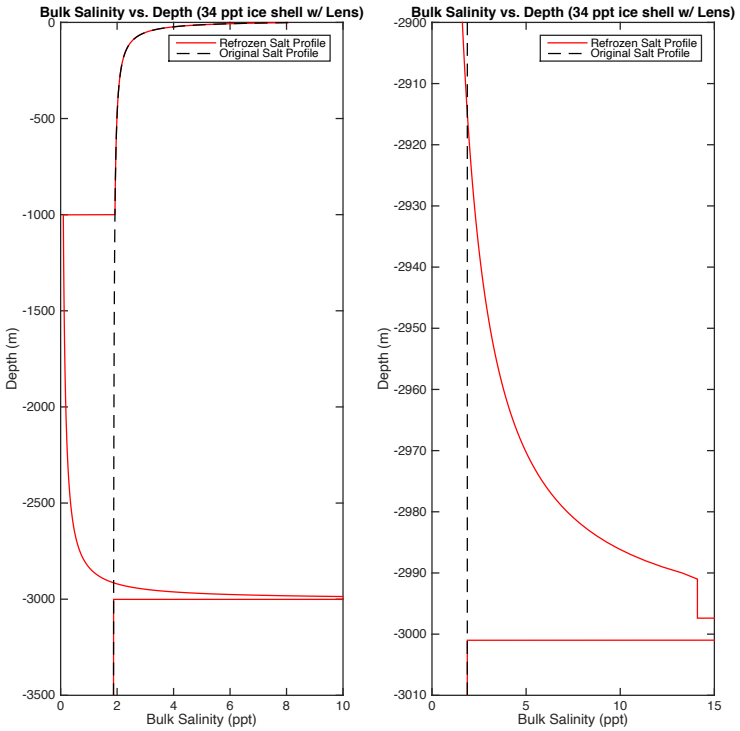

Figure 5: Bulk salinity profile of a perched water lens upon re-solidification. Left) A 2 km thick lens is assumed to form via the *in situ* melting of a preexisting ice shell, whose original composition is given by the black dashed line. Initially the lens salinity is less than that of the original ocean, but upon top down solidification salt is concentrated in the remaining liquid phase, leading to an increase in ice bulk salinity [red line] near the base of the refrozen lens as well as ~2.23 m of precipitated salt on the lens floor (1000 ppt values excluded from plot). **Right)** A magnified view of ice bulk salinity near the bottom of the lens (2.90 – 3.01 km). The lens saturates (282 ppt) when the ice reaches 2991 m, resulting in salt precipitation (2997.77 – 3000 m). 733

734

735 **4. Discussion**

736 We explicitly quantify the overall impurity content of Europa's ice shell, suggesting an
737 average composition (total salt/ice shell mass) of between 1.053 and 14.72 ppt of non-ice material
738 (depending on ocean composition). We extend the general notion that Europa's ice shell contains
739 ocean-derived impurities [*Kargel et al.*, 2000; *Zolotov and Kargel*, 2009] by providing two
740 methods (direct modeling and constitutive equations) to predict the spatiotemporal distribution of
741 salts within the shell. Our estimates of the ice shell's bulk salinity, predictions of concentrated salt
742 layers near hydrological features within the shell, numerical models, and constitutive equations
743 can be included in more realistic models of the geophysical evolution of the ice shell.

744 Compositional heterogeneities can either aid or prevent buoyancy driven convection in the
745 ductile region of the ice shell, which is important for constraining the rates of subduction and
746 surface recycling [*Howell and Pappalardo*, 2019; *Johnson et al.*, 2017b; *Kattenhorn*, 2018].
747 Additionally, salts affect the rheological properties of the ice, especially relative to pure water ice,
748 which impacts its mechanical behavior [*Durham et al.*, 2010; *Durham et al.*, 2005]. Our estimates
749 of material entrainment at the ice-ocean interface will aid in predicting the thermo-compositional
750 convection dynamics in the ductile region of the shell (e.g. [*Barr and McKinnon*, 2007; *Han and*
751 *Showman*, 2005; *Pappalardo and Barr*, 2004]) and help quantify ocean-surface material transport
752 rates (e.g. [*Allu Peddinti and McNamara*, 2015]). These transport rates feed forward into the
753 putative reductant-oxidant cycle associated with ocean-surface interaction [*Vance et al.*, 2016], by
754 which ice shell overturn delivers surface-generated oxidants and ice-shell derived chemical species
755 as potential energy sources to the ocean. Constraining chemical cycling associated with ice shell
756 overturn and ocean-surface interaction is a fundamental component of assessing the habitability of

Europa and other ice-ocean worlds [*Des Marais et al.*, 2008; *Hendrix et al.*, 2019; *Pappalardo et al.*, 2017; *Schmidt*, 2020]. Furthermore, determining the lifetime of liquid water features within the ice shell is of profound importance in considering whether such reservoirs could be putative habitats; relevant for both planetary exploration and planetary protection [*Board and Council*, 2012a; *Schmidt*, 2020]. While our models suggest that shallow subsurface water in a conductive ice shell is short lived, the warmer, isothermal regime of an ice shell undergoing convection may provide an environment where hydrological features could persist for much longer.

Our results also demonstrate regions of high material contrast associated with hydrological features within the ice shell that could promote or extend geologic activity and provide an observable indicator of past or present liquid environments. We have shown that the rate of ice formation is directly related to the entrainment of salts, suggesting that when fluids intruded into the ice shell contact the cold surrounding ice, they will form rinds of high salinity ice. These highly distinct layers will have fundamentally different thermal and mechanical properties than the background ice shell, making them susceptible to reactivation through stress concentration or eutectic melting. Our results will improve estimates of fracture mechanics on Europa (e.g. [*Craft et al.*, 2016; *Walker et al.*, (in revision)]) and aid in determining if frictionally generated melts can be produced in active fractures (e.g. [*Kalousová et al.*, 2014; 2016]) by informing physicochemical and structural models of these features. We have shown that impurity entrainment leads to the concentration of isolated hydrological features within the shell, such as lenses, to the point that they can reach their saturation limit and precipitate layers of pure hydrated salts. Our estimates of lens evolution (Section 3.3.3) are the first to include the chemical evolution of the water bodies and can be used to improve estimates of their longevity (e.g. [*Chivers et al.*, 2020; *Michaut and Manga*, 2014]) and habitability [*Schmidt*, 2020], as the composition of the fluid impacts both the freezing point of the fluid and biologically important properties such as water activity and chaotropicity [*Oren*, 2013; *Pontefract et al.*, 2019; *Pontefract et al.*, 2017]. The high salt contents associated with both fractures and lenses make them prime candidates for detection by ice penetrating radar instruments (e.g. RIME onboard JUICE, REASON onboard Europa Clipper), as salt substantially alters the dielectric properties of ice (e.g. [*Blankenship et al.*, 2009; *Schroeder et al.*, 2016]). Our model's ability to simulate the physicochemical evolution of the ice that forms in and around hydrological features provides a means to predict the dielectric structure of both the features and background ice shell. These dielectric profiles can be used as an inversion tool (e.g. [*Kalousová et al.*, 2017]) once radar observations have been made to constrain the structure, composition, and evolution of remnant and relict hydrological features.

5. Conclusion

The impurity load and distribution of entrained ocean materials within Europa's ice shell impacts the evolution of the ice shell, Europa's geology, and interactions between the surface and the ocean. Compositional profiles of the bulk ice shell and geologic features effectively capture the thermal and physicochemical nature of the ice that can be observed by Europa Clipper's remote sensing and radar instruments: the spatial distribution of impurities on the surface and the dielectric properties of the ice and water within the shell carry with them an accessible fingerprint of ice shell dynamics and the ocean below.

Acknowledgments

General

The authors thank Sven Simon (Georgia Institute of Technology) for helpful discussions regarding the analytical solution of the modified Stefan Problem.

Funding

This study was supported by the NASA Earth and Space Science Fellowship, grant NNX16AP43H S01 and NNX16AP43H S002. Britney Schmidt was additionally supported by the Europa Clipper Mission. Resources supporting this work were provided by the NASA High-End Computing (HEC) Program through the NASA Advanced Supercomputing (NAS) Division at Ames Research Center.

Author Contributions

J. J. B. contributed in designing the research, constructing the multiphase reactive transport model, carrying out the research, interpreting the results, and writing/reviewing the paper.
B. E. S. contributed in designing the research, interpreting the results, and writing/reviewing the paper.
C. H. contributed in constructing the multiphase reactive transport model, interpreting the results, and writing/reviewing the paper.
C. C. W. contributed in constructing the fracture mechanics model, interpreting results, and writing/reviewing the paper.

Competing Interests

The authors declare no competing financial nor non-financial interests.

Materials and Correspondence

Code Availability

Liquidus 1.0 and its associated documentation can be found at: DOI: 10.5281/zenodo.3774072
SlushFund 2.0 and its associated documentation can be found at: DOI: 10.5281/zenodo.3774078

All correspondence and material requests should be made to Jacob J. Buffo at: jacob.j.buffo@dartmouth.edu

References

Allu Peddinti, D., and A. K. McNamara (2015), Material transport across Europa's ice shell, *Geophysical Research Letters*, *42*(11), 4288-4293.

Barr, A. C., and W. B. McKinnon (2007), Convection in ice I shells and mantles with self-consistent grain size, *Journal of Geophysical Research: Planets*, *112*(E2).

Bassis, J., and C. Walker (2011), Upper and lower limits on the stability of calving glaciers from the yield strength envelope of ice, *Proc. R. Soc. A*, rspa20110422.

Billings, S. E., and S. A. Kattenhorn (2005), The great thickness debate: Ice shell thickness models for Europa and comparisons with estimates based on flexure at ridges, *Icarus*, *177*(2), 397-412.

Blankenship, D. D., D. A. Young, W. B. Moore, and J. C. Moore (2009), Radar sounding of Europa's subsurface properties and processes: The view from Earth, *Europa. University of Arizona Press, Tucson, AZ*.

Board, S. S., and N. R. Council (2012a), *Assessment of Planetary Protection Requirements for Spacecraft Missions to Icy Solar System Bodies*, National Academies Press.

Board, S. S., and N. R. Council (2012b), *Vision and voyages for planetary science in the decade 2013-2022*, National Academies Press.

Brown, E. K., et al. (2020), TRAPPED IN THE ICE: AN ANALYSIS OF BRINES IN BRITISH COLUMBIA'S HYPERSALINE LAKES, in *Lunar and Planetary Science Conference*, edited, Woodlands, TX.

Buffo, J., B. Schmidt, and C. Huber (2018), Multiphase reactive transport and platelet ice accretion in the sea ice of McMurdo sound, Antarctica, *Journal of Geophysical Research: Oceans*, *123*(1), 324-345.

Buffo, J. J. (2019), Multiphase reactive transport in planetary ices, Georgia Institute of Technology.

Butler, B. M., S. Papadimitriou, A. Santoro, and H. Kennedy (2016), Mirabilite solubility in equilibrium sea ice brines, *Geochimica et Cosmochimica Acta*, *182*, 40-54.

Carr, M. H., M. J. Belton, C. R. Chapman, M. E. Davies, P. Geissler, R. Greenberg, A. S. McEwen, B. R. Tufts, R. Greeley, and R. Sullivan (1998), Evidence for a subsurface ocean on Europa, *Nature*, *391*(6665), 363.

Cassen, P., R. T. Reynolds, and S. Peale (1979), Is there liquid water on Europa?, *Geophysical Research Letters*, *6*(9), 731-734.

Charette, M. A., and W. H. Smith (2010), The volume of Earth's ocean, *Oceanography*, *23*(2), 112-114.

Chivers, C., J. Buffo, and B. Schmidt (2020), Thermal and Chemical Evolution of Small, Shallow Water Bodies on Europa, *LPI*(2326), 1047.

Chu, H., G. Chi, and I. M. Chou (2016), Freezing and melting behaviors of H2O-NaCl-CaCl2 solutions in fused silica capillaries and glass-sandwiched films: implications for fluid inclusion studies, *Geofluids*, *16*(3), 518-532.

Chyba, C. F., and C. B. Phillips (2001), Possible ecosystems and the search for life on Europa, *Proceedings of the National Academy of Sciences*, *98*(3), 801-804.

Collins, G., and F. Nimmo (2009), Chaotic terrain on Europa, in *Europa*, edited, pp. 259-281, University of Arizona Press Tucson.

Commission, I. O. (2010), The International thermodynamic equation of seawater–2010: calculation and use of thermodynamic properties.[includes corrections up to 31st October 2015].

Cox, G., and W. Weeks (1988), Numerical simulations of the profile properties of undeformed first-year sea ice during the growth season, *Journal of Geophysical Research: Oceans*, *93*(C10), 12449-12460.

Craft, K. L., G. W. Patterson, R. P. Lowell, and L. Germanovich (2016), Fracturing and flow: Investigations on the formation of shallow water sills on Europa, *Icarus*, *274*, 297-313.

Craven, M., I. Allison, H. A. Fricker, and R. Warner (2009), Properties of a marine ice layer under the Amery Ice Shelf, East Antarctica, *Journal of Glaciology*, *55*(192), 717-728.

Davis, N., and P. Wadhams (1995), A statistical analysis of Arctic pressure ridge morphology, *Journal of Geophysical Research: Oceans*, *100*(C6), 10915-10925.

Des Marais, D. J., J. A. Nuth III, L. J. Allamandola, A. P. Boss, J. D. Farmer, T. M. Hoehler, B. M. Jakosky, V. S. Meadows, A. Pohorille, and B. Runnegar (2008), The NASA astrobiology roadmap, *Astrobiology*, *8*(4), 715-730.

Dickson, A. G., and C. Goyet (1994), Handbook of methods for the analysis of the various parameters of the carbon dioxide system in sea water. Version 2*Rep.*, Oak Ridge National Lab., TN (United States).

Durham, W., O. Prieto-Ballesteros, D. Goldsby, and J. Kargel (2010), Rheological and thermal properties of icy materials, *Space Science Reviews*, *153*(1-4), 273-298.

Durham, W. B., L. A. Stern, T. Kubo, and S. H. Kirby (2005), Flow strength of highly hydrated Mg-and Na-sulfate hydrate salts, pure and in mixtures with water ice, with application to Europa, *Journal of Geophysical Research: Planets*, *110*(E12).

Eicken, H. (2003), From the microscopic, to the macroscopic, to the regional scale: growth, microstructure and properties of sea ice, *Sea ice: an introduction to its physics, chemistry, biology and geology*, 22-81.

Fagents, S. A. (2003), Considerations for effusive cryovolcanism on Europa: The post-Galileo perspective, *Journal of Geophysical Research: Planets*, *108*(E12).

Feltham, D., N. Untersteiner, J. Wettlaufer, and M. Worster (2006), Sea ice is a mushy layer, *Geophysical Research Letters*, *33*(14).

Galton-Fenzi, B., J. Hunter, R. Coleman, S. Marsland, and R. Warner (2012), Modeling the basal melting and marine ice accretion of the Amery Ice Shelf, *Journal of Geophysical Research: Oceans*, *117*(C9).

Golden, K., S. Ackley, and V. Lytle (1998), The percolation phase transition in sea ice, *Science*, *282*(5397), 2238-2241.

Golden, K. M., H. Eicken, A. Heaton, J. Miner, D. Pringle, and J. Zhu (2007), Thermal evolution of permeability and microstructure in sea ice, *Geophysical Research Letters*, *34*(16).

Greenberg, R., G. V. Hoppa, B. Tufts, P. Geissler, J. Riley, and S. Kadel (1999), Chaos on Europa, *Icarus*, *141*(2), 263-286.

Griewank, P. J., and D. Notz (2013), Insights into brine dynamics and sea ice desalination from a 1-D model study of gravity drainage, *Journal of Geophysical Research: Oceans*, *118*(7), 3370-3386.

Gross, G. W., P. M. Wong, and K. Humes (1977), Concentration dependent solute redistribution at the ice–water phase boundary. III. Spontaneous convection. Chloride solutions, *The Journal of chemical physics*, *67*(11), 5264-5274.

Han, L., and A. P. Showman (2005), Thermo-compositional convection in Europa's icy shell with salinity, *Geophysical research letters*, *32*(20).

Hand, K. P., and C. F. Chyba (2007), Empirical constraints on the salinity of the europan ocean and implications for a thin ice shell, *Icarus*, *189*(2), 424-438.

941 Hendrix, A. R., T. A. Hurford, L. M. Barge, M. T. Bland, J. S. Bowman, W. Brinckerhoff, B. J.
942 Buratti, M. L. Cable, J. Castillo-Rogez, and G. C. Collins (2019), The NASA Roadmap
943 to Ocean Worlds, *Astrobiology*, *19*(1), 1-27.
944 Howell, S. M., and R. T. Pappalardo (2018), Band formation and ocean-surface interaction on
945 Europa and Ganymede, *Geophysical Research Letters*, *45*(10), 4701-4709.
946 Howell, S. M., and R. T. Pappalardo (2019), Can Earth-like plate tectonics occur in ocean world
947 ice shells?, *Icarus*, *322*, 69-79.
948 Huber, C., A. Parmigiani, B. Chopard, M. Manga, and O. Bachmann (2008), Lattice Boltzmann
949 model for melting with natural convection, *International Journal of Heat and Fluid Flow*,
950 *29*(5), 1469-1480.
951 Hunke, E., D. Notz, A. Turner, and M. Vancoppenolle (2011), The multiphase physics of sea ice:
952 a review for model developers, *The Cryosphere*, *5*(4), 989-1009.
953 Huppert, H. E., and M. G. Worster (1985), Dynamic solidification of a binary melt, *Nature*,
954 *314*(6013), 703.
955 Johnson, B. C., R. Y. Sheppard, A. C. Pascuzzo, E. A. Fisher, and S. E. Wiggins (2017a),
956 Porosity and Salt Content Determine if Subduction Can Occur in Europa's Ice Shell,
957 *Journal of Geophysical Research: Planets*, *122*(12), 2765-2778.
958 Johnson, B. C., R. Y. Sheppard, A. C. Pascuzzo, E. A. Fisher, and S. E. Wiggins (2017b),
959 Porosity and Salt Content Determine if Subduction Can Occur in Europa's Ice Shell,
960 *Journal of Geophysical Research: Planets*.
961 Kalousová, K., D. M. Schroeder, and K. M. Soderlund (2017), Radar attenuation in Europa's ice
962 shell: Obstacles and opportunities for constraining the shell thickness and its thermal
963 structure, *Journal of Geophysical Research: Planets*, *122*(3), 524-545.
964 Kalousová, K., O. Souček, G. Tobie, G. Choblet, and O. Čadek (2014), Ice melting and
965 downward transport of meltwater by two-phase flow in Europa's ice shell, *Journal of*
966 *Geophysical Research: Planets*, *119*(3), 532-549.
967 Kalousová, K., O. Souček, G. Tobie, G. Choblet, and O. Čadek (2016), Water generation and
968 transport below Europa's strike-slip faults, *Journal of Geophysical Research: Planets*,
969 *121*(12), 2444-2462.
970 Kargel, J. S., J. Z. Kaye, J. W. Head III, G. M. Marion, R. Sassen, J. K. Crowley, O. P.
971 Ballesteros, S. A. Grant, and D. L. Hogenboom (2000), Europa's crust and ocean: origin,
972 composition, and the prospects for life, *Icarus*, *148*(1), 226-265.
973 Kattenhorn, S. A. (2018), Commentary: The Feasibility of Subduction and Implications for Plate
974 Tectonics on Jupiter’s moon Europa.
975 Kattenhorn, S. A., and L. M. Prockter (2014), Evidence for subduction in the ice shell of Europa,
976 *Nature Geoscience*, *7*(10), 762.
977 Khazendar, A., E. Rignot, and E. Larour (2009), Roles of marine ice, rheology, and fracture in
978 the flow and stability of the Brunt/Stancomb-Wills Ice Shelf, *Journal of Geophysical*
979 *Research: Earth Surface*, *114*(F4).
980 Khurana, K., M. Kivelson, D. Stevenson, G. Schubert, C. Russell, R. Walker, and C. Polanskey
981 (1998), Induced magnetic fields as evidence for subsurface oceans in Europa and
982 Callisto, *Nature*, *395*(6704), 777.
983 Kivelson, M. G., K. K. Khurana, C. T. Russell, M. Volwerk, R. J. Walker, and C. Zimmer
984 (2000), Galileo magnetometer measurements: A stronger case for a subsurface ocean at
985 Europa, *Science*, *289*(5483), 1340-1343.

Kurtz, N., and T. Markus (2012), Satellite observations of Antarctic sea ice thickness and volume, *Journal of Geophysical Research: Oceans*, *117*(C8).

Laxon, S. W., K. A. Giles, A. L. Ridout, D. J. Wingham, R. Willatt, R. Cullen, R. Kwok, A. Schweiger, J. Zhang, and C. Haas (2013), CryoSat-2 estimates of Arctic sea ice thickness and volume, *Geophysical Research Letters*, *40*(4), 732-737.

Lyon, W. (1961), DIVISION OF OCEANOGRAPHY AND METEOROLOGY: OCEAN AND SEA-ICE RESEARCH IN THE ARCTIC OCEAN VIA SUBMARINE, *Transactions of the New York Academy of Sciences*, *23*(8 Series II), 662-674.

Malmgren, F., and G. Institutt (1927), *On the properties of sea-ice*, AS John Griegs Boktrykkeri.

Manga, M., and C. Michaut (2017), Formation of lenticulae on Europa by saucer-shaped sills, *Icarus*, *286*, 261-269.

Marion, G. M., J. S. Kargel, D. C. Catling, and S. D. Jakubowski (2005), Effects of pressure on aqueous chemical equilibria at subzero temperatures with applications to Europa, *Geochimica et Cosmochimica Acta*, *69*(2), 259-274.

McCarthy, C., J. Blackford, and C. Jeffree (2013), Low-temperature-SEM study of dihedral angles in the ice-I/sulfuric acid partially molten system, *Journal of microscopy*, *249*(2), 150-157.

McCarthy, C., R. F. Cooper, D. L. Goldsby, W. B. Durham, and S. H. Kirby (2011), Transient and steady state creep response of ice I and magnesium sulfate hydrate eutectic aggregates, *Journal of Geophysical Research: Planets*, *116*(E4).

McCarthy, C., R. F. Cooper, S. H. Kirby, K. D. Rieck, and L. A. Stern (2007), Solidification and microstructures of binary ice-I/hydrate eutectic aggregates, *American Mineralogist*, *92*(10), 1550-1560.

McCarthy, C., M. A. Nielson, A. N. Coonin, J. S. Minker, and A. A. Domingos (2019), Acoustic and Microstructural Properties of Partially Molten Samples in the Ice–Ammonia System, *Geosciences*, *9*(8), 327.

McCord, T. B., G. B. Hansen, D. L. Matson, T. V. Johnson, J. K. Crowley, F. P. Fanale, R. W. Carlson, W. D. Smythe, P. D. Martin, and C. A. Hibbitts (1999), Hydrated salt minerals on Europa's surface from the Galileo near-infrared mapping spectrometer (NIMS) investigation, *Journal of Geophysical Research: Planets*, *104*(E5), 11827-11851.

McCord, T. B., G. Teeter, G. B. Hansen, M. T. Sieger, and T. M. Orlando (2002), Brines exposed to Europa surface conditions, *Journal of Geophysical Research: Planets*, *107*(E1), 4-1-4-6.

McKinnon, W. B. (1999), Convective instability in Europa's floating ice shell, *Geophysical Research Letters*, *26*(7), 951-954.

McKinnon, W. B., and M. E. Zolensky (2003), Sulfate content of Europa's ocean and shell: Evolutionary considerations and some geological and astrobiological implications, *Astrobiology*, *3*(4), 879-897.

Michaut, C., and M. Manga (2014), Domes, pits, and small chaos on Europa produced by water sills, *Journal of Geophysical Research: Planets*, *119*(3), 550-573.

Mitri, G., and A. P. Showman (2005), Convective–conductive transitions and sensitivity of a convecting ice shell to perturbations in heat flux and tidal-heating rate: Implications for Europa, *Icarus*, *177*(2), 447-460.

Nakawo, M., and N. K. Sinha (1981), Growth rate and salinity profile of first-year sea ice in the high Arctic, *Journal of Glaciology*, *27*(96), 315-330.

1031 Nakawo, M., and N. K. Sinha (1984), A note on brine layer spacing of first-year sea ice,
1032 *Atmosphere-ocean*, *22*(2), 193-206.
1033 Nimmo, F., and E. Gaidos (2002), Strike-slip motion and double ridge formation on Europa,
1034 *Journal of Geophysical Research: Planets*, *107*(E4), 5-1-5-8.
1035 Nimmo, F., B. Giese, and R. Pappalardo (2003), Estimates of Europa's ice shell thickness from
1036 elastically-supported topography, *Geophysical Research Letters*, *30*(5).
1037 Notz, D., and M. G. Worster (2009), Desalination processes of sea ice revisited, *Journal of*
1038 *Geophysical Research: Oceans*, *114*(C5).
1039 Oren, A. (2013), Life in magnesium-and calcium-rich hypersaline environments: salt stress by
1040 chaotropic ions, in *Polyextremophiles*, edited, pp. 215-232, Springer.
1041 Pappalardo, R., M. Belton, H. Breneman, M. Carr, C. Chapman, G. Collins, T. Denk, S. Fagents,
1042 P. Geissler, and B. Giese (1999), Does Europa have a subsurface ocean? Evaluation of
1043 the geological evidence, *Journal of Geophysical Research: Planets*, *104*(E10), 24015-
1044 24055.
1045 Pappalardo, R., D. Senske, H. Korth, R. Klima, S. Vance, and K. Craft (2017), The Europa
1046 Clipper Mission: Exploring The Habilatbility of A Unique Icy World, paper presented at
1047 European Planetary Science Congress.
1048 Pappalardo, R. T., and A. C. Barr (2004), The origin of domes on Europa: The role of thermally
1049 induced compositional diapirism, *Geophysical Research Letters*, *31*(1).
1050 Phillips, C. B., and R. T. Pappalardo (2014), Europa Clipper mission concept: Exploring Jupiter's
1051 ocean moon, *Eos, Transactions American Geophysical Union*, *95*(20), 165-167.
1052 Pontefract, A., C. E. Carr, and M. R. Osburn (2019), The Role of Ionic Composition and
1053 Concentration on Biosignature Preservation: Lessons from the “Spotted” Lakes of British
1054 Colombia, paper presented at 2019 Astrobiology Science Conference, AGU.
1055 Pontefract, A., T. F. Zhu, V. K. Walker, H. Hepburn, C. Lui, M. T. Zuber, G. Ruvkun, and C. E.
1056 Carr (2017), Microbial diversity in a hypersaline sulfate lake: a terrestrial analog of
1057 ancient Mars, *Frontiers in microbiology*, *8*, 1819.
1058 Renaut, R. W., and P. R. Long (1989), Sedimentology of the saline lakes of the Cariboo plateau,
1059 Interior British Columbia, Canada, *Sedimentary Geology*, *64*(4), 239-264.
1060 Reynolds, R. T., S. W. Squyres, D. S. Colburn, and C. P. McKay (1983), On the habitability of
1061 Europa, *Icarus*, *56*(2), 246-254.
1062 Ross, M., and G. Schubert (1987), Tidal heating in an internal ocean model of Europa, *Nature*,
1063 *325*(6100), 133-134.
1064 Rubinšteĭn, L. (2000), *The stefan problem*, American Mathematical Soc.
1065 Russell, M. J., A. E. Murray, and K. P. Hand (2017), The possible emergence of life and
1066 differentiation of a shallow biosphere on irradiated icy worlds: the example of Europa,
1067 *Astrobiology*, *17*(12), 1265-1273.
1068 Schmidt, B. (2020), The Astrobiology of Europa and the Jovian System, *Planetary Astrobiology*,
1069 185.
1070 Schmidt, B. E., D. D. Blankenship, G. W. Patterson, and P. M. Schenk (2011), Active formation
1071 of 'chaos terrain' over shallow subsurface water on Europa, *Nature*, *479*(7374), 502-505,
1072 doi:10.1038/nature10608.
1073 Schroeder, D. M., A. Romero-Wolf, L. Carrer, C. Grima, B. A. Campbell, W. Kofman, L.
1074 Bruzzone, and D. D. Blankenship (2016), Assessing the potential for passive radio
1075 sounding of Europa and Ganymede with RIME and REASON, *Planetary and Space*
1076 *Science*, *134*, 52-60.

Soderlund, K., B. Schmidt, J. Wicht, and D. Blankenship (2014), Ocean-driven heating of Europa's icy shell at low latitudes, *Nature Geoscience*, *7*(1), 16.

Sparks, W. B., B. E. Schmidt, M. A. McGrath, K. P. Hand, J. Spencer, M. Cracraft, and S. E. Deustua (2017), Active cryovolcanism on Europa?, *The Astrophysical Journal Letters*, *839*(2), L18.

Squyres, S. W., R. T. Reynolds, P. M. Cassen, and S. J. Peale (1983), Liquid water and active resurfacing on Europa, *Nature*, *301*(5897), 225-226.

Thomas, E. C., R. Hodyss, T. H. Vu, P. V. Johnson, and M. Choukroun (2017), Composition and evolution of frozen chloride brines under the surface conditions of Europa, *ACS Earth and Space Chemistry*, *1*(1), 14-23.

Tobie, G., G. Choblet, and C. Sotin (2003), Tidally heated convection: Constraints on Europa's ice shell thickness, *Journal of Geophysical Research: Planets*, *108*(E11).

Toner, J., D. Catling, and B. Light (2014), The formation of supercooled brines, viscous liquids, and low-temperature perchlorate glasses in aqueous solutions relevant to Mars, *Icarus*, *233*, 36-47.

Turner, A. K., and E. C. Hunke (2015), Impacts of a mushy-layer thermodynamic approach in global sea-ice simulations using the CICE sea-ice model, *Journal of Geophysical Research: Oceans*, *120*(2), 1253-1275.

Turner, A. K., E. C. Hunke, and C. M. Bitz (2013), Two modes of sea-ice gravity drainage: A parameterization for large-scale modeling, *Journal of Geophysical Research: Oceans*, *118*(5), 2279-2294.

Untersteiner, N. (1968), Natural desalination and equilibrium salinity profile of perennial sea ice, *Journal of Geophysical Research*, *73*(4), 1251-1257.

Vance, S., K. Hand, and R. Pappalardo (2016), Geophysical controls of chemical disequilibria in Europa, *Geophysical Research Letters*, *43*(10), 4871-4879.

Vance, S. D., L. M. Barge, S. S. Cardoso, and J. H. Cartwright (2019), Self-Assembling Ice Membranes on Europa: Brinicle Properties, Field Examples, and Possible Energetic Systems in Icy Ocean Worlds, *arXiv preprint arXiv:1903.01584*.

Walker, C., and B. Schmidt (2015), Ice collapse over trapped water bodies on Enceladus and Europa, *Geophysical Research Letters*, *42*(3), 712-719.

Walker, C. C., J. N. Bassis, and B. E. Schmidt ((in revision)), Propagation of vertical fractures through planetary ice shells and the role of basal cracks at the ice-ocean interface, *Earth and Planetary Science Letters*.

Weeks, W., and G. Lofgren (1967), The effective solute distribution coefficient during the freezing of NaCl solutions, *Physics of Snow and Ice: proceedings= 雪氷の物理学: 論文集*, *1*(1), 579-597.

Weeks, W. F., and S. F. Ackley (1986), The growth, structure, and properties of sea ice, in *The geophysics of sea ice*, edited, pp. 9-164, Springer.

Wells, A., J. Wettlaufer, and S. Orszag (2011), Brine fluxes from growing sea ice, *Geophysical Research Letters*, *38*(4).

Worster, M. G. (1991), Natural convection in a mushy layer, *Journal of fluid mechanics*, *224*, 335-359.

Worster, M. G., and D. W. Rees Jones (2015), Sea-ice thermodynamics and brine drainage, *Philosophical Transactions of the Royal Society A: Mathematical, Physical and Engineering Sciences*, *373*(2045), 20140166.

Zolotov, M. Y., and J. Kargel (2009), *On the chemical composition of Europa's icy shell, ocean, and underlying rocks*, University of Arizona Press Tucson, AZ.

Zolotov, M. Y., and E. L. Shock (2001), Composition and stability of salts on the surface of Europa and their oceanic origin, *Journal of Geophysical Research: Planets*, *106*(E12), 32815-32827.

Zotikov, I. A., V. S. Zagorodnov, and J. V. Raikovsky (1980), Core drilling through the Ross Ice Shelf (Antarctica) confirmed basal freezing, *Science*, *207*(4438), 1463-1465.